Journal of Engineering Mathematics **38:** 191–218, 2000.
© 2000 *Kluwer Academic Publishers. Printed in the Netherlands.*

Oxidation-induced stresses in the isolation oxidation of silicon

J. D. EVANS[1]*, M. VYNNYCKY[2] and S. P. FERRO[3]
[1]*Department of Mathematics, The University of Wales, Aberystwyth, Ceredigion, SY23 3BZ, UK (E-mail: masjde@maths.bath.ac.uk)*
[2]*Department of Mechanics, Royal Institute of Technology, S-100 44 Stockholm, Sweden*
[3]*INFIP-CONICET, Departamento de Fisica, Universidad de Buenos Aires, Pab. 1, Ciudad Universitaria, 1428 Buenos Aires, Argentina*

Received 1 April 1997; accepted in revised form 3 September 1999

Abstract. The two-dimensional isolation oxidation of silicon is studied in the reaction-controlled limit, which corresponds to the case of initially thin oxides. This limit is both of physical relevance and one of the few regimes in which analytical progress can be made in the whole oxide region. Slowly-varying or long-wave approximations can be used to derive equations that govern the growth of the oxide interfaces (which form two moving boundaries) and the oxidation-induced stresses in the oxide. Here, these equations are solved numerically, by use of a Keller-Box discretisation scheme, complementing previously obtained asymptotic results. The numerical scheme is used to investigate the effects of the nitride-cap rigidity and the initial oxide thickness on both the lateral extent of oxidation (the so-called 'bird's beak' length) and the stresses that occur on the silicon/silicon-oxide interface. The results from the model are interpreted in dimensional form so that quantitative comparisons can be made with experimental results.

Key words: silicon oxidation, oxidation-induced stresses, numerical finite differences, Keller-Box discretisation scheme

1. Introduction

The local oxidation of silicon (LOCOS) is a well-studied process (first reported by Appels *et al.* [1]) in which oxide is selectively grown on part of a silicon wafer during the fabrication of an integrated circuit. This selective oxidation is achieved by masking the parts of the silicon surface where devices will be formed with silicon nitride and then growing the oxide (known as the field oxide) by the thermal oxidation of the unmasked silicon, the nitride being impervious to oxidant. Before the deposition of the nitride mask, a thin oxide (known as the pad oxide) is grown on the silicon in order to reduce the stresses that result from the different thermal expansion coefficients of the silicon and the nitride. Since an oxidant is able to diffuse laterally under the mask through the pad oxide, the resulting oxide has a characteristic shape known as a bird's beak. The model equations for the two-dimensional problem of this process are discussed in detail in King [2, 3] and these describe a moving boundary problem commonly termed the bird's beak problem (see also Tayler and King [4]). The important goals of the modelling are to determine conditions that minimize both the lateral extent of oxidation (the length of the bird's beak) and the oxidation-induced stresses. An asymptotic analysis of the model equations in the reaction-controlled case is given in King [5]. Here we complete the analysis of the reaction-controlled case by providing numerical results which complement the

*Author to whom correspondence should be addressed. Present address: Department of Mathematical Sciences, University of Bath, Bath, BA2 7AY, United Kingdom.

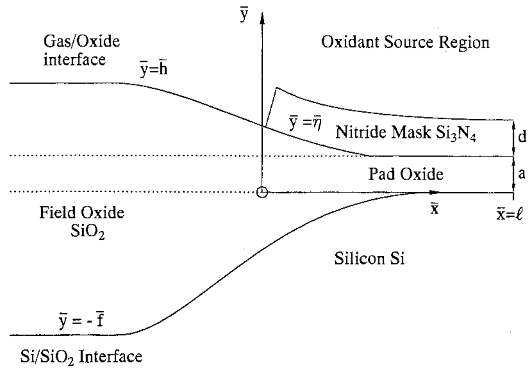

Figure 1. The bird's beak geometry during local oxidation. The pad oxide thickness is a cm (or $a \times 10^8$ Å), whilst the nitride mask has thickness d cm (or $d \times 10^8$ Å) and half length ℓ cm (or $\ell \times 10^4$ μm). The silicon/oxide interface is at $\bar{y} = -\bar{f}(\bar{x}, \bar{t})$ for $-\infty < \bar{x} < \ell$ and the nitride/oxide interface is at $\bar{y} = \bar{\eta}(\bar{x}, \bar{t})$ for $0 < \bar{x} < \ell$. The problem is assumed symmetric about the symmetry boundary $\bar{x} = \ell$.

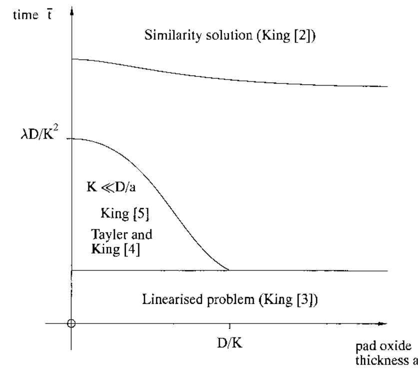

Figure 2. A schematic summarising the times and initial oxide thicknesses in which analytical results may be obtained in the whole oxide region. The reaction-controlled limit corresponds to the region where $K \ll D/a$.

previously obtained asymptotics, and then interpreting the results in dimensional form. The layout of the paper is as follows:
In the remainder of the introduction, a summary of the previous analytical work by King [3, 5] is given; the system of equations describing the growth of the interfaces and stresses are stated together with their important similarity solutions and asymptotic results. Numerical schemes for these systems of equations are presented in Section 2, which are based upon a Keller-Box discretisation scheme. In Section 3, the numerical schemes are used to determine validity ranges for the asymptotic results summarised in the introduction and to investigate the parametric dependence of the stresses. Finally, Section 4 interprets the results obtained in Section 3 in dimensional form, by providing values for the dimensional parameters and comparing them to results obtained experimentally.

The important geometry is shown in Figure 1, where the two moving boundaries are the oxide/silicon interface $\bar{y} = -\bar{f}(\bar{x}, \bar{t})$ and the nitride/oxide interface $\bar{y} = \bar{\eta}(\bar{x}, \bar{t})$ or the oxide/gas interface $\bar{y} = \bar{h}(\bar{x}, \bar{t})$ (depending on location). The variables stated are dimensional, with $\overline{x}$ and $\overline{y}$ being horizontal and vertical distances, $\bar{t}$ time, a cm (or $a \times 10^8$ Å) denoting the initial pad oxide thickness, d cm (or $d \times 10^8$ Å) the nitride mask thickness and 2ℓ cm (or $2\ell \times 10^4\mu$m) is the total length of the nitride mask. In the reaction-controlled limit (see King [5]), the following dimensionless variables are introduced,

$$y = \frac{\overline{y}}{a}, \quad X = \epsilon \frac{\overline{x}}{a}, \quad \tau = \epsilon^2 \frac{D}{a^2 \lambda} \bar{t},$$

together with the $O(1)$ dimensionless parameters

$$\kappa = \epsilon^{-2} \frac{Ka}{D}, \quad R_2 = \epsilon^4 \frac{\lambda EI}{\mu Da}, \quad H = \frac{\overline{H}a}{D}.$$

Here D (cm^2/s) is the diffusivity coefficient of the oxidant through the oxide, $\underline{K}$ (cm/s) is the reaction coefficient for the first-order reaction at the silicon/oxide interface, $\overline{H}$ (cm/s) is the gas-phase transport coefficient, μ (poise) is the viscosity of the oxide and EI (Pa cm^3) is the flexural rigidity of the nitride mask. The parameter $\lambda = N/\gamma c^*$ is dimensionless where c^* (cm^{-3}) is the equilibrium concentration of the oxidant in the oxide, and N (cm^{-3}) denotes the number of oxidant molecules that combine with a unit volume of silicon to form a volume $\gamma \approx 2{\cdot}25$ of oxide. It is this net volume expansion of $\gamma - 1 \approx 1{\cdot}25$ which drives the flow of the oxide and gives rise to the deformation of the nitride/oxide and gas/oxide interfaces. The parameter ϵ is small and is that used for the perturbative analysis. Since $\kappa = O(1)$ this corresponds to the case $a \ll D/K$ where the initial pad oxide thickness is small compared to the length scale D/K. This is termed the reaction-controlled case. King [5] derives the following coupled problem for the leading-order growth of the boundaries in the region $X \geq 0$ (under the nitride mask),

$$\kappa f_{0\tau} = \left((\eta_0 + f_0) f_{0_{X\tau}}\right)_X \ , \tag{1.1}$$

$$\eta_{0\tau} - (\gamma - 1) f_{0\tau} = \frac{R_2}{12}\left((\eta_0 + f_0)^3 \eta_{0_{XXXXX}}\right)_X \ , \tag{1.2}$$

$$\text{at } X = 0\text{:} \quad f_0 = \frac{\kappa}{\gamma}\tau \ , \ \eta_{0_{XX}} = \eta_{0_{XXX}} = \eta_{0_{XXXX}} = 0 \ , \tag{1.3}$$

$$\text{as } X \to \infty\text{:} \quad f_0 \to 0, \ \eta_0 \to 1 \ , \tag{1.4}$$

$$\text{at } \tau = 0\text{:} \quad f_0 = 0 \ , \quad \eta_0 = 1 \ , \tag{1.5}$$

where $f_0(X,\tau)$ denotes the leading-order term (in a regular expansion in powers of ϵ) of the silicon/silicon oxide boundary and $\eta_0(X,\tau)$ denotes the leading-order term of the nitride/silicon oxide boundary, *i.e.* $f \sim f_0(X,\tau) + O(\epsilon)$ and $\eta \sim \eta_0(X,\tau) + O(\epsilon)$ are posed for $X \geq 0$. The linear growth condition for the silicon/silicon oxide interface imposed at the nitride mask edge $X = 0$ follows from the one-dimensional Deal and Grove [6] solution, which is assumed to hold in the field oxide. Specifically, $\bar{f} \sim a\hat{f}(\tau)$ and $\bar{h} \sim a\left((\gamma - 1)\hat{f} + 1\right)$ in $X < 0$ where $\hat{f}$ is the positive root of

$$\frac{1}{2}\gamma^2 \hat{f}^2 + \left(1 + \frac{1}{H} + \frac{\epsilon^2}{\kappa}\right)\gamma \hat{f} = \epsilon^{-2}\tau \ , \tag{1.6}$$

which upon expanding in regular powers of ϵ gives

$$\hat{f} \sim \frac{\kappa\tau}{\gamma} - \epsilon^2\kappa\left[\left(1 + \frac{1}{H}\right)\frac{\kappa\tau}{\gamma} + \frac{\kappa^2\tau^2}{2\gamma}\right] \tag{1.7}$$

with the linear growth condition at leading order. The leading-order stresses under the nitride mask are as follows,

$$\sigma_{11}, \sigma_{22} \sim -R_2 \eta_{0_{XXXX}} \ , \quad \sigma_{12} \sim \epsilon R_2 \eta_{0_{XXXXX}}\left(-y + \tfrac{1}{2}(\eta_0 - f_0)\right) \ , \tag{1.8}$$

where σ_{ij} is a suitably scaled dimensionless stress tensor (see Section 4) with 1 denoting the X-direction and 2 the y-direction. The stresses are $O(1)$ and larger than those at the mask edge and in the field oxide which are only $O(\epsilon)$. It is worth mentioning that the nitride mask is treated as semi-infinite, the relevance of this assumption is considered in Section 3.3.

The system (1.1)–(1.5) further simplifies for the cases of small nitride rigidity ($R_2 \to 0$) and large nitride rigidity ($R_2 \to \infty$), which are discussed in Appendix A. These limits are important as they provide the greatest and least extents of lateral oxidation respectively. In both cases the governing equation for the growth of the silicon/silicon oxide interface can be written in the form,

$$f_t = ((1 + f) f_{xt})_x \ , \tag{1.9}$$

with

$$\text{at } x = 0 \qquad f = t \ , \tag{1.10}$$

$$\text{as } x \to \infty \qquad f \to 0 \ , \tag{1.11}$$

$$\text{at } t = 0 \qquad f = 0 \ , \tag{1.12}$$

under the scalings

$$f = \gamma f_1 \ , \quad t = \kappa \tau \ , \quad x = \sqrt{\kappa} X \ , \tag{1.13}$$

for small nitride rigidity where f_1 is now the leading order position of the silicon/oxide interface, and

$$f = f_3 \ , \quad t = \frac{\kappa}{\gamma} \tau \ , \quad x = \sqrt{\kappa} X \ , \tag{1.14}$$

for large nitride rigidity, where f_3 denotes the leading-order position of the silicon/oxide interface.

It is known that (1.9)–(1.12) possesses a travelling wave solution of varying speed (King [3, 5]), the implicit solution being given by

$$\int_f^t \frac{\mathrm{d}u}{(u - \log(1 + u))^{1/2}} = \sqrt{2} x \ . \tag{1.15}$$

This solution, when expresssed in terms of the travelling wave variable $z = x - d(t)$, takes the form

$$z = \frac{1}{\sqrt{2}} \int_f^1 \frac{\mathrm{d}u}{(u - \log(1 + u))^{1/2}} \ , \tag{1.16}$$

where

$$d(t) = \frac{1}{\sqrt{2}} \int_t^1 \frac{\mathrm{d}u}{(u - \log(1 + u))^{1/2}} \tag{1.17}$$

denotes the position of the front of the travelling wave (taken to be where f=1). If the scalings (1.13) and (1.14) are used, this defines the wave fronts $d_1(\tau) = d(\kappa\tau)/\sqrt{\kappa}$ and $d_3(\tau) = d(\kappa\tau/\gamma)/\sqrt{\kappa}$ in the small and large nitride rigidity cases, respectively.

Finally, (1.7) shows that the reaction-controlled case remains valid until $\tau = O(\epsilon^{-2})$, corresponding to dimensional times $O(\lambda D/K^2)$ s, which is when the slowly-varying approximations and the expansion in (1.7) are expected to breakdown. Figure 2 indicates the extent of validity of the reaction-controlled case and summarises other limits for which analytical results can be obtained for the whole oxide region in terms of time and initial oxide thickness.

2. Numerical methods

In this section finite-difference schemes are presented for the numerical solution of the two types of evolution equations stated in Section 1. These two systems of partial differential equations are central in describing the growth of the boundaries and the development of the oxidation-induced stresses within the oxide.

For both evolution equations, we adopt the Keller-Box discretisation scheme and solve the resulting nonlinear algebraic equations using Newton iteration (see, for example, Cebeci and Bradshaw [7]); the scheme, which is second-order accurate in both time-like and space-like variables, is perhaps more familiar in the solution of thermal and viscous boundary-layer equations, so that its application in the present context warrants further explanation, as follows.

2.1. A 'PSEUDO-PARABOLIC' EQUATION

Writing $f_t = g$ in the governing Equation (1.9), and further introducing $h = g_x$, we note that (1.9) can be written as three first-order differential equations, that is

$$h = g_x, \quad g = ((1 + f)\,h)_x\,, \quad f_t = g. \tag{2.1–3}$$

Introducing a rectangular mesh with grid points at $(x_i)_{i=0,\ldots,N}$ and $(t_j)_{j=0,1,..}$, and consequently with mesh spacing

$$\Delta x_i = x_i - x_{i-1}, \quad i = 1,\ldots, N, \quad \Delta t_j = t_j - t_{j-1}, \quad j = 1,\ldots,$$

we discretise (2.1) and (2.2) about $(x_{i-\frac{1}{2}}, t_{j+1})$, and (2.3) about $(x_{i-\frac{1}{2}}, t_{j+\frac{1}{2}})$, to obtain the following finite-difference forms:

$$\frac{1}{2}\left(h_{i,j+1} + h_{i-1,j+1}\right) = \frac{g_{i,j+1} - g_{i-1,j+1}}{\Delta x_i}, \tag{2.4}$$

$$\frac{1}{2}\left(g_{i,j+1} + g_{i-1,j+1}\right) = \frac{\left(1 + f_{i,j+1}\right) h_{i,j+1} - \left(1 + f_{i-1,j+1}\right) h_{i-1,j+1}}{\Delta x_i}, \tag{2.5}$$

$$\frac{f_{i-\frac{1}{2},j+1} - f_{i-\frac{1}{2},j}}{\Delta t_j} = \frac{1}{2}\left(g_{i-\frac{1}{2},j+1} + g_{i-\frac{1}{2},j}\right), \tag{2.6}$$

where, for any variable ϕ , $\phi_{i-\frac{1}{2},k} = \frac{1}{2}\left(\phi_{i,k} + \phi_{i-1,k}\right)$.

Introducing the iterates $\phi^{(n)}_{i,j+1}$, $n = 0, 1, 2, \ldots$, where n denotes the iteration order, we set for the higher iterates

$$\phi^{(n)}_{i,j+1} = \phi^{(n-1)}_{i,j+1} + \delta\phi_i \ . \tag{2.7}$$

Inserting into (2.4)–(2.6) and linearising gives for $i = 1, \ldots, N$,

$$-\left(\frac{2}{\Delta x_i}\right)\delta g_i + \left(\frac{2}{\Delta x_i}\right)\delta g_{i-1} + \delta h_i + \delta h_{i-1} = \mathcal{R}^{(n)}_{1,i} \ , \tag{2.8}$$

$$-\frac{2h^{(n)}_{i,j+1}}{\Delta x_i}\delta f_i + \frac{2h^{(n)}_{i-1,j+1}}{\Delta x_i}\delta f_{i-1} + \delta g_i + \delta g_{i-1}$$
$$-\frac{2(1+f^{(n)}_{i,j+1})}{\Delta x_i}\delta h_i + \frac{2(1+f^{(n)}_{i-1,j+1})}{\Delta x_i}\delta h_{i-1} = \mathcal{R}^{(n)}_{2,i}, \tag{2.9}$$

$$\left(\frac{1}{\Delta t_j}\right)\delta f_i + \left(\frac{1}{\Delta t_j}\right)\delta f_{i-1} - \left(\frac{1}{2}\right)\delta g_i - \left(\frac{1}{2}\right)\delta g_{i-1} = \mathcal{R}^{(n)}_{3,i}, \tag{2.10}$$

where

$$\mathcal{R}^{(n)}_{1,i} = \frac{2}{\Delta x_i}\left(g^{(n)}_{i,j+1} - g^{(n)}_{i-1,j+1}\right) - \left(h^{(n)}_{i,j+1} + h^{(n)}_{i-1,j+1}\right),$$

$$\mathcal{R}^{(n)}_{2,i} = -\left(g^{(n)}_{i,j+1} + g^{(n)}_{i-1,j+1}\right) + \frac{2}{\Delta x_i}\left\{\left(1 + f^{(n)}_{i,j+1}\right)h^{(n)}_{i,j+1} - \left(1 + f^{(n)}_{i-1,j+1}\right)h^{(n)}_{i-1,j+1}\right\},$$

$$\mathcal{R}^{(n)}_{3,i} = -\frac{2\left(f^{(n)}_{i-\frac{1}{2},j+1} - f_{i-\frac{1}{2},j}\right)}{\Delta t_j} + \left(g^{(n)}_{i-\frac{1}{2},j+1} + g_{i-\frac{1}{2},j}\right).$$

For the numerical scheme, three boundary conditions are required in order to supplement the $3N$ algebraic equations given by (2.8)-(2.10), for the $3N+3$ unknowns $(\delta f_i, \delta g_i, \delta h_i)_{i=0,\ldots,N}$. Although (1.10) and (1.11) suggest only two conditions, a third may be deduced from (2.3); so, we have

$$f_{0,j+1} = t_{j+1}, \quad f_{N,j+1} = 0, \quad g_{0,j+1} = 1, \tag{2.11–13}$$

which lead to

$$\delta f_0 = 0, \quad \delta f_N = 0, \quad \delta g_0 = 0. \tag{2.14–16}$$

As for the initial conditions, it is clear that, as $t \to 0$, (2.2) reduces to

$$g = g_{xx}, \tag{2.17}$$

with the solution, subject to boundary conditions,

$$g = \mathrm{e}^{-x}. \tag{2.18}$$

Thus, we arrive at

$$f_{i,0} = 0, \quad g_{i,0} = \mathrm{e}^{-x_i}, \quad h_{i,0} = -\mathrm{e}^{-x_i}. \tag{2.19–21}$$

The above scheme gives a block tridiagonal system of equations to be solved for the iterates $(\delta f_i, \delta g_i, \delta h_i)_{i=0,\dots,N}$ at the $(j+1)$th time step. Typically, the convergence criterion

$$\max_{i=0,\dots,N} (\delta f_i, \delta g_i, \delta h_i) < 10^{-9}$$

on the Newton iteration was found to be satisfied after 3 or 4 iterations. Additional comments concerning the numerical scheme, in particular the discretisations used and the size of the computational domain, are relegated to the end of Section 2.2.

2.2. A SIXTH-ORDER EVOLUTION EQUATION

Writing $f_{0\tau} = g$, and introducing

$$\eta_m = \eta_0^{(m)}(X), \quad m = 1, \dots, 5,$$

where here the superscript denotes the order of the derivative with respect to X, we may write (1.1) and (1.2) as nine first-order differential equations, as follows:

$$\eta_m = \eta_{m-1X}, \quad m = 1, \dots, 5, \tag{2.22}$$

$$h = g_X, \quad \kappa g = ((\eta_0 + f_0)\, h)_X\,, \quad f_{0\tau} = g, \tag{2.23–25}$$

$$\eta_{0\tau} - (\gamma - 1)\, g = \frac{R_2}{12} \left((\eta_0 + f_0)^3\, \eta_5\right)_X. \tag{2.26}$$

Introducing a rectangular mesh with grid points at $(X_i)_{i=0,\dots,N}$ and $(\tau_j)_{j=0,1,\dots}$, and consequently with mesh spacing

$$\Delta X_i = X_i - X_{i-1}, \quad i = 1, \dots, N; \quad \Delta\tau_j = \tau_j - \tau_{j-1}, \quad j = 1, \dots,$$

we find that these become, in finite-difference form,

$$\frac{1}{2}\left(\left[\eta_m\right]_{i,j+1} + \left[\eta_m\right]_{i-1,j+1}\right) = \frac{\left[\eta_{m-1}\right]_{i,j+1} - \left[\eta_{m-1}\right]_{i-1,j+1}}{\Delta X_i}, \quad \text{for } m = 1, \dots, 5, \tag{2.27}$$

$$\frac{1}{2}\left(h_{i,j+1} + h_{i-1,j+1}\right) = \frac{g_{i,j+1} - g_{i-1,j+1}}{\Delta X_i}, \tag{2.28}$$

$$\frac{\kappa}{2}\left(g_{i,j+1} + g_{i-1,j+1}\right) =$$

$$\frac{\left(\left[\eta_0\right]_{i,j+1} + \left[f_0\right]_{i,j+1}\right) h_{i,j+1} - \left(\left[\eta_0\right]_{i-1,j+1} + \left[f_0\right]_{i-1,j+1}\right) h_{i-1,j+1}}{\Delta X_i}, \tag{2.29}$$

$$\frac{\left[f_0\right]_{i-\frac{1}{2},j+1} - \left[f_0\right]_{i-\frac{1}{2},j}}{\Delta\tau_j} = \frac{1}{2}\left(g_{i-\frac{1}{2},j+1} + g_{i-\frac{1}{2},j}\right), \tag{2.30}$$

$$\frac{\left[\eta_0\right]_{i-\frac{1}{2},j+1} - \left[\eta_0\right]_{i-\frac{1}{2},j}}{\Delta\tau_j} - \frac{(\gamma-1)}{2}\left(g_{i-\frac{1}{2},j+1} + g_{i-\frac{1}{2},j}\right) =$$

$$\frac{R_2}{12}\left\{\frac{\left([\eta_0]_{i,j+1}+[f_0]_{i,j+1}\right)^3[\eta_5]_{i,j+1}-\left([\eta_0]_{i-1,j+1}+[f_0]_{i-1,j+1}\right)^3[\eta_5]_{i-1,j+1}}{2\Delta X_i}\right.$$

$$\left.+\frac{\left([\eta_0]_{i,j}+[f_0]_{i,j}\right)^3[\eta_5]_{i,j}-\left([\eta_0]_{i-1,j}+[f_0]_{i-1,j}\right)^3[\eta_5]_{i-1,j}}{2\Delta X_i}\right\}. \tag{2.31}$$

At this stage, it would appear that we are once again heading for a block tridiagonal system, albeit that the blocks are now 9×9, rather than 3×3 as before. Indeed, this was the scheme that was initially tried, before it became apparent that it was impossible to obtain convergence for the Newton iterations. Consequently, it became necessary to break up (2.27)–(2.31) into a third-order system consisting of (2.28)–(2.30), and a sixth-order system consisting of (2.27) and (2.31); thus, one system was solved to convergence, its results substituted in the other, which was then also solved to convergence and its results substituted in the first, and so on until convergence for the outer loop was obtained. Further details are as follows.

Introducing the iterates for the functions $f_0, g, h, [\eta_m]_{m=0,..,5}$ as

$$[f_0]^{(\nu,n)}_{i,j+1}=[f_0]^{(\nu,n-1)}_{i,j+1}+\delta[f_0]_i\,,$$

$$g^{(\nu,n)}_{i,j+1}=g^{(\nu,n-1)}_{i,j+1}+\delta g_i,\quad h^{(\nu,n)}_{i,j+1}=h^{(\nu,n-1)}_{i,j+1}+\delta h_i,$$

$$[\eta_m]^{(\nu,n)}_{i,j+1}=[\eta_m]^{(\nu,n-1)}_{i,j+1}+\delta[\eta_m]_i\,,\quad m=0,\ldots,5,$$

where ν denotes the order of the outer iterative loop and n denotes the order of the inner iterative loop, we have at the νth outer step, after linearising,

$$-\left(\frac{2}{\Delta X_i}\right)\delta g_i+\left(\frac{2}{\Delta X_i}\right)\delta g_{i-1}+\delta h_i+\delta h_{i-1}=\mathcal{R}^{(\nu,n)}_{6,i}, \tag{2.32}$$

$$-\left(\frac{2h^{(\nu,n)}_{i,j+1}}{\Delta X_i}\right)\delta[f_0]_i+\left(\frac{2h^{(\nu,n)}_{i-1,j+1}}{\Delta X_i}\right)\delta[f_0]_{i-1}+\kappa\delta g_i+\kappa\delta g_{i-1}$$

$$-\frac{2}{\Delta X_i}\left([\eta_0]^{(\nu-1)}_{i,j+1}+[f_0]^{(\nu,n)}_{i,j+1}\right)\delta h_i+\frac{2}{\Delta X_i}\left([\eta_0]^{(\nu-1)}_{i-1,j+1}+[f_0]^{(\nu,n)}_{i-1,j+1}\right)\delta h_{i-1}$$

$$-\left(\frac{2h^{(\nu,n)}_{i,j+1}}{\Delta X_i}\right)\delta[\eta_0]_i+\left(\frac{2h^{(\nu,n)}_{i-1,j+1}}{\Delta X_i}\right)\delta[\eta_0]_{i-1}=\mathcal{R}^{(\nu,n)}_{7,i}, \tag{2.33}$$

$$\left(\frac{1}{\Delta\tau_j}\right)\delta[f_0]_i+\left(\frac{1}{\Delta\tau_j}\right)\delta[f_0]_{i-1}-\left(\frac{1}{2}\right)\delta g_i-\left(\frac{1}{2}\right)\delta g_{i-1}=\mathcal{R}^{(\nu,n)}_{8,i}, \tag{2.34}$$

where

$$\mathcal{R}^{(\nu,n)}_{6,i}=\frac{2}{\Delta X_i}\left(g^{(\nu,n)}_{i,j+1}-g^{(\nu,n)}_{i-1,j+1}\right)-\left(h^{(\nu,n)}_{i,j+1}+h^{(\nu,n)}_{i-1,j+1}\right),$$

$$\mathcal{R}_{7,i}^{(\nu,n)} = -\kappa\left(g_{i,j+1}^{(\nu,n)} + g_{i-1,j+1}^{(\nu,n)}\right) + \frac{2}{\Delta X_i}\left\{\left([\eta_0]_{i,j+1}^{(\nu-1)} + [f_0]_{i,j+1}^{(\nu,n)}\right)h_{i,j+1}^{(\nu,n)} - \left([\eta_0]_{i-1,j+1}^{(\nu-1)} + [f_0]_{i-1,j+1}^{(\nu,n)}\right)h_{i-1,j+1}^{(\nu,n)}\right\},$$

$$\mathcal{R}_{8,i}^{(\nu,n)} = -\frac{2\left([f_0]_{i-\frac{1}{2},j+1}^{(\nu,n)} - [f_0]_{i-\frac{1}{2},j}\right)}{\Delta\tau_j} + \left(g_{i-\frac{1}{2},j+1}^{(\nu,n)} + g_{i-\frac{1}{2},j}\right),$$

and $[\eta_0]_{i,j+1}^{(\nu-1)}$ denotes the converged solution for η_0 after the $(\nu-1)$st outer iteration. Having found $[f_0]_{i,j+1}^{(\nu)}$, $g_{i,j+1}^{(\nu)}$, $h_{i,j+1}^{(\nu)}$, we move to

$$\delta\left[\eta_m\right]_i + \delta\left[\eta_m\right]_{i-1} - \left(\frac{2}{\Delta X_i}\right)\delta\left[\eta_{m-1}\right]_i + \left(\frac{2}{\Delta X_i}\right)\delta\left[\eta_{m-1}\right]_{i-1} = \mathcal{R}_{m,i}^{(\nu,n)}, \quad m = 1, ..., 5, \tag{2.35}$$

$$\begin{aligned}
&-\left\{\frac{R_2}{4\Delta X_i}\left([\eta_0]_{i,j+1}^{(\nu,n)} + [f_0]_{i,j+1}^{(\nu)}\right)^2 [\eta_5]_{i,j+1}^{(\nu,n)}\right\}\delta\left[f_0\right]_i \\
&+\left\{\frac{R_2}{4\Delta X_i}\left([\eta_0]_{i-1,j+1}^{(\nu,n)} + [f_0]_{i-1,j+1}^{(\nu)}\right)^2 [\eta_5]_{i-1,j+1}^{(\nu,n)}\right\}\delta\left[f_0\right]_{i-1} - \frac{(\gamma-1)}{2}\delta g_i - \frac{(\gamma-1)}{2}\delta g_{i-1} \\
&+\left\{\frac{1}{\Delta\tau_j} - \frac{R_2}{4\Delta X_i}\left([\eta_0]_{i,j+1}^{(\nu,n)} + [f_0]_{i,j+1}^{(\nu)}\right)^2 [\eta_5]_{i,j+1}^{(\nu,n)}\right\}\delta\left[\eta_0\right]_i \\
&+\left\{\frac{1}{\Delta\tau_j} - \frac{R_2}{4\Delta X_i}\left([\eta_0]_{i-1,j+1}^{(\nu,n)} + [f_0]_{i-1,j+1}^{(\nu)}\right)^2 [\eta_5]_{i-1,j+1}^{(\nu,n)}\right\}\delta\left[\eta_0\right]_{i-1} \\
&-\frac{R_2\left([\eta_0]_{i,j+1}^{(\nu,n)} + [f_0]_{i,j+1}^{(\nu)}\right)^3}{12\Delta X_i}\delta\left[\eta_5\right]_i + \frac{R_2\left([\eta_0]_{i-1,j+1}^{(\nu,n)} + [f_0]_{i-1,j+1}^{(\nu)}\right)^3}{12\Delta X_i}\delta\left[\eta_5\right]_{i-1} = \mathcal{R}_{9,i}^{(\nu,n)},
\end{aligned} \tag{2.36}$$

where

$$\mathcal{R}_{m,i}^{(\nu,n)} = \frac{2}{\Delta X_i}\left([\eta_{m-1}]_{i,j+1}^{(\nu,n)} - [\eta_{m-1}]_{i-1,j+1}^{(\nu,n)}\right) - \left([\eta_m]_{i,j+1}^{(\nu,n)} + [\eta_m]_{i-1,j+1}^{(\nu,n)}\right), \quad m = 1, \ldots, 5,$$

$$\begin{aligned}
\mathcal{R}_{9,i}^{(\nu,n)} = &-\frac{2}{\Delta\tau_j}\left([\eta_0]_{i-\frac{1}{2},j+1}^{(\nu,n)} - [\eta_0]_{i-\frac{1}{2},j}\right) + (\gamma-1)\left(g_{i-\frac{1}{2},j+1}^{(\nu)} + g_{i-\frac{1}{2},j}\right) \\
&+\frac{R_2}{12\Delta X_i}\left\{\left(\left[\eta_0\right]_{i,j+1}^{(\nu,n)} + \left[f_0\right]_{i,j+1}^{(\nu)}\right)^3\left[\eta_5\right]_{i,j+1}^{(\nu,n)} - \left(\left[\eta_0\right]_{i-1,j+1}^{(\nu,n)} + \left[f_0\right]_{i-1,j+1}^{(\nu)}\right)^3\left[\eta_5\right]_{i-1,j+1}^{(\nu,n)}\right. \\
&\left.+\left(\left[\eta_0\right]_{i,j} + \left[f_0\right]_{i,j}\right)^3\left[\eta_5\right]_{i,j} - \left(\left[\eta_0\right]_{i-1,j} + \left[f_0\right]_{i-1,j}\right)^3\left[\eta_5\right]_{i-1,j}\right\}.
\end{aligned}$$

This time, nine boundary conditions are required to supplement the $9N$ equations for the $9N + 9$ unknowns. Equations (1.3) and (1.4) give six of the required conditions:

$$[f_0]_{0,j+1} = \frac{\kappa\tau_{j+1}}{\gamma}, \quad [\eta_2]_{0,j+1} = [\eta_3]_{0,j+1} = [\eta_4]_{0,j+1} = 0, \tag{2.37}$$

$$[f_0]_{N,j+1} = 0, [\eta_0]_{N,j+1} = 1. \tag{2.38–39}$$

As in Section 2.1, we may use the conditions on f_0 at $X = 0$ and as $X \to \infty$ to derive two boundary conditions for g, namely

$$g_{0,j+1} = \frac{\kappa}{\gamma}, \quad g_{N,j+1} = 0; \tag{2.40–41}$$

as a final boundary condition, we set

$$[\eta_1]_{N,j+1} = 0. \tag{2.42}$$

Subsequently, (2.37)–(2.42) reduce to zero boundary conditions:

$$\delta[f_0]_0 = 0, \quad \delta[\eta_2]_0 = \delta[\eta_3]_0 = \delta[\eta_4]_0 = 0, \tag{2.43}$$

$$\delta[f_0]_N = 0, \quad \delta[\eta_0]_N = 0, \tag{2.44–45}$$

$$\delta g_0 = 0, \quad \delta g_N = 0, \quad \delta[\eta_1]_N = 0, \tag{2.46–48}$$

As for initial conditions, (1.5) gives conditions on seven of the variables:

$$[f_0]_{i,0} = 0, \quad [\eta_0]_{i,0} = 1, \quad [\eta_m]_{i,0} = 0, \quad \text{for } m = 1, ..., 5, \tag{2.49}$$

for $i = 0, .., N$. For g and h, we require the solution to (2.24) as $\tau \to 0$, that is

$$\kappa g = g_{XX}, \tag{2.50}$$

subject to

$$g = \frac{\kappa}{\gamma} \quad \text{at } X = 0, \quad g \to 0 \quad \text{as } X \to \infty; \tag{2.51–52}$$

thence

$$g = \frac{\kappa}{\gamma}\mathrm{e}^{-\kappa^{\frac{1}{2}}X},$$

so that, for $i = 0, .., N$,

$$g_{i,0} = \frac{\kappa}{\gamma}\mathrm{e}^{-\kappa^{\frac{1}{2}}X_i}, \quad h_{i,0} = -\frac{\kappa^{\frac{3}{2}}}{\gamma}\mathrm{e}^{-\kappa^{\frac{1}{2}}X_i}. \tag{2.53–54}$$

The convergence criteria employed here were, for the inner iterations,

$$\max_{i=0,.,N} (\delta[f_0]_i, \delta g_i, \delta h_i) < 10^{-9},$$

$$\max_{i=0,..,N;m=0,..,5}(\delta[\eta_m]_i) < 10^{-9},$$

whilst for the outer iterations we use

$$\max_{i=0,..,N}\Big(|\,[f_0]^{(\nu)}_{i,j+1}-[f_0]^{(\nu-1)}_{i,j+1}\,|,|\,g^{(\nu)}_{i,j+1}-g^{(\nu-1)}_{i,j+1}\,|,$$

$$|\,h^{(\nu)}_{i,j+1}-h^{(\nu-1)}_{i,j+1}\,|,\Big(|\,[\eta_m]^{(\nu)}_{i,j+1}-[\eta_m]^{(\nu-1)}_{i,j+1}\,|\Big)_{m=0,..,5}\Big) < 10^{-9};$$

3 or 4 iterations were found to suffice for both the inner and outer iterative steps. In general, for the computations of this subsection and Section 2.1, uniform dimensionless time steps of 10^{-2} were used. However, since one of the goals of this work was to determine both maximum and minimum stresses, which for high values of R_2 were found to occur for values of dimensionless time less than 10^{-2}, numerical integrations of the equations of this subsection were started with dimensionless time steps of 10^{-4}. A further comment here concerns the discretisation in space, and in particular the setting of the outer edge (X_∞) of the computational domain. From the analysis in Section 1, it is clear that the solution is in the form of travelling wave, and it is thus necessary to ensure that, for a given integration end-time (τ_{end}, say), the peak of the wave has not reached X_∞; consequently, higher values of τ_{end} require higher values of X_∞. This situation is of course in contrast to that for viscous boundary layers where there is no such wave. As an example of these considerations, we note that the results in Figures 4a and 5a were obtained with $X_\infty = 40$ and $\tau_{\text{end}} = 500$; for the discretisation in space, uniform spacing with $N = 1001$ was used.

When $\kappa = 0$ in (1.1), (1.2) gives the sixth-order parabolic equation $\eta_{0_\tau} = (\eta_0^3\eta_{0_{XXXXX}})_X$ which is yet another equation in a hierarchy of nonlinear partial differential equations describing the motion of thin viscous droplets under different forces (see King [5]). The numerical scheme presented may be used for this sixth-order equation and can be modified to deal with the lower fourth- and second-order variants which arise when the driving forces are surface tension and gravity respectively in place of the light plate.

3. Numerical results

We are particularly interested in the growth of the oxide/nitride and the oxide/silicon boundaries, and the behaviour of the largest stresses which occur under the nitride mask. The growth of the interfaces will be bounded by those for the small and large nitride rigidity which we discuss first, before considering the oxide stresses.

3.1. Asymptotic approximations for the interface growth

The silicon/oxide and oxide/nitride interfaces are bounded by those in the small and large nitride rigidity cases, namely

$$f_3(X,\tau) \le f_0(X,\tau) \le f_1(X,\tau) \quad \text{and} \quad \eta_3(X,\tau) \le \eta_0(X,\tau) \le \eta_1(X,\tau)$$

where, as discussed in Appendix A, $\eta_3 \equiv 1$ and $\eta_1 = 1 + (\gamma - 1)f_1(X,\tau)$ for $X \ge 0$ and $\tau \ge 0$. There are different definitions of the bird's beak length (see Poncet [8]), but here it is taken as the distance from the nitride-mask edge to where the oxide thickness has doubled

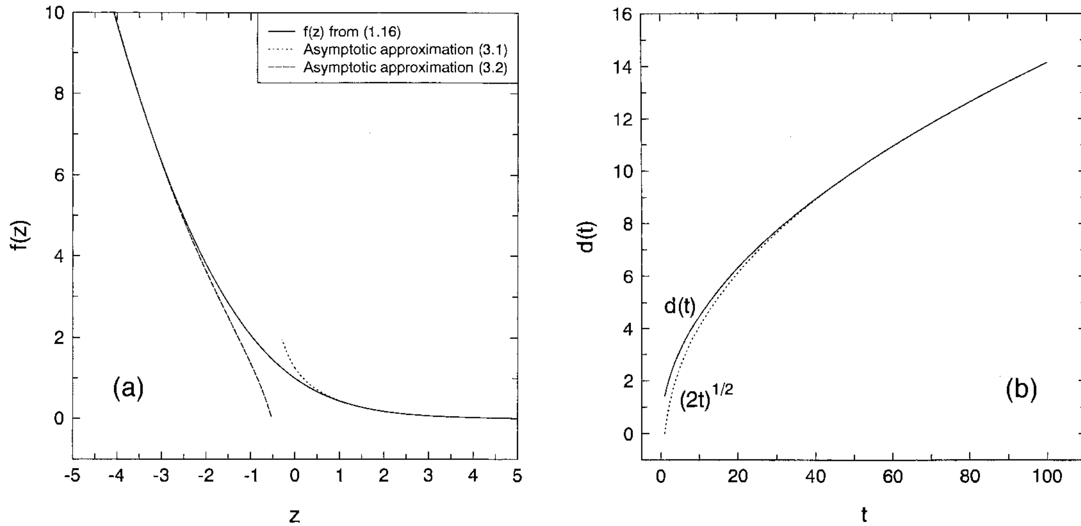

Figure 3. Plots of the travelling wave solution and the location of its front. (a) shows the solution $f(z)$ from (1.16) together with the asymptotic approximations (3.1) and (3.2). (b) shows the location of the front of the travelling-wave solution $d(t)$ from (1.17) together with the large-time asymptotic solution $\sqrt{2t}$.

from its initial thickness. Since $\eta_1 + f_1 = 2$ at $\gamma f_1 = 1$ and $\eta_3 + f_3 = 2$ at $f_3 = 1$, the functions $d_1(\tau)$ and $d_3(\tau)$, given at the end of Section 1, thus characterize the bird's beak length in the small and large nitride rigidity cases, respectively; the extent of lateral oxidation being greatest in the small rigidity case and least in the large rigidity case.

The travelling-wave solution (1.16) has the following asymptotic behaviours,

$$f \sim a_0 e^{-z} - \frac{a_0^2}{3} e^{-2z} + \frac{5a_0^3}{24} e^{-3z} \quad \text{as } z \to +\infty\ , \tag{3.1}$$

$$f \sim \frac{z^2}{2} - \sqrt{2} a_1 z + 2\log(-z) + 2 + a_1^2 - \log 2 \quad \text{as } z \to -\infty\ , \tag{3.2}$$

where the constants $a_0 \approx 1{\cdot}35$ and $a_1 \approx -0{\cdot}45$ are determined numerically. These asymptotic behaviours are shown in Figure 3a and are good approximations for $-2 < z < 0{\cdot}5$, covering most of the range of the travelling wave variable.

The large-time behaviour of (1.9)–(1.12) or equivalently (1.15), is derived in Appendix B and is a moving parabola, whose front is located at $\sqrt{2t}$ (*i.e.* $\sqrt{2\tau}$ and $\sqrt{2\tau/\gamma}$ for the small and large rigidity cases, respectively). The outer (moving-parabola) solution

$$f \sim t\left(1 - \frac{x}{\sqrt{2t}}\right)^2\ , \tag{3.3}$$

is a reasonable approximation for $x < \sqrt{2t} - 5$, the solution then after being given by $f \sim r_0$ where

$$\int_{r_0}^{1{\cdot}607} \frac{\mathrm{d}u}{(u - \log(1+u))^{1/2}} = \sqrt{2}\left(x - \sqrt{2t}\right)\ . \tag{3.4}$$

Figure 3b shows the position of the travelling-wave front $d(t)$ from (1.17) and the large-time behaviour $\sqrt{2t}$. This indicates that the large-time approximation begins to be valid for $t \geq O(50)$ (*i.e.* $\tau \geq O(100/\kappa)$ for small nitride rigidity and $\tau \geq O(100\gamma/\kappa)$ for large nitride rigidity), although we would not expect the outer moving-parabola solution to emerge to form a significant part of the large-time solution until much later. The outer solution would be expected to be valid for approximately $(\sqrt{2t}-5)/\sqrt{2t}$ fraction of the large-time behaviour solution.

3.2. Oxide stresses

Of particular importance during the oxidation process are the oxidation-induced stresses in the oxide. If these stresses are too large, dislocations may be generated in the silicon substrate with detrimental effects on device operation. In this section we present the numerical results for the leading-order stress terms stated in (1.8) and their dependence on the nitride rigidity parameter R_2. Although the shear or tangential stress σ_{12} is seen to be an order of magnitude smaller than the normal stresses σ_{11} and σ_{22}, it is often the resolved values of the shear stresses that are critical in determining the generation of dislocations (Tamura and Sunami [9], Isomae [10] and Isomae and Yamamoto [11]) and for this reason we investigate its behaviour as well.

The main region of interest is under the mask in $X = O(1)$, where largest stresses are expected to occur compared to the mask edge and field oxide regions. Since the parameter κ can be removed from the problem by a suitable rescaling of the other variables and the parameter R_2, it is sufficient to consider the case $\kappa = 1$ and the dependence of the stresses on the nitride rigidity parameter R_2 only. Figure 4a shows the development of $\eta_{0_{XXXX}}$ with time for the parameter value $R_2 = 1$. Figure 4b shows the dependence of the maximum and minimum value of $R_2\eta_{0_{XXXX}}$ with R_2, whilst Figures 4c and 4d shows the position and time when the maximum and minimum occur, which we note are not continuous with R_2, this suggesting that there is a certain region where the minimum stresses are of greater absolute magnitude than the maximum stresses. The oscillatory behaviour of the normal stresses is not unexpected since the total normal force exerted on the nitride mask must be zero at leading order. Physically, the plus and minus signs of the normal stresses correspond to tensile and compressive stresses, respectively.

Figure 5a shows the development of the scaled shear stress σ_{12}/ϵ on the silicon/oxide interface $y = -f_0$ and gives an indication of its oscillatory behaviour. Figures 5b, 5c and 5d show the maximum and minimum values of the shear stress on the silicon/oxide interface and the position and time when these maximum and minimum values occur, the position of the maximum shear stress always occurring at $X = 0$. Again, there are similar qualitative features as in the normal stress case, where the position of the minimum stress occurs further under the mask as the rigidity increases although in this case the maximum always occurring at the mask edge $X = 0$ and the largest stresses occurring at progressively earlier times for increasing mask rigidity.

3.2.1. *Small nitride rigidity*

Considering the limit $R_2 \to 0$ for small nitride rigidity, it is observed from Figures 4b and 5b that the maximum and minimum values of the stresses become smaller, whilst Figures 4c and 5c show that their positions occur nearer to the nitride mask edge in agreement with the results of the asymptotics derived in Appendix A. It is in this case that the lateral extent of oxidation is the greatest, with the bird's beak length being characterised by $d_1(\tau) = d(\kappa\tau)/\sqrt{\kappa}$, with

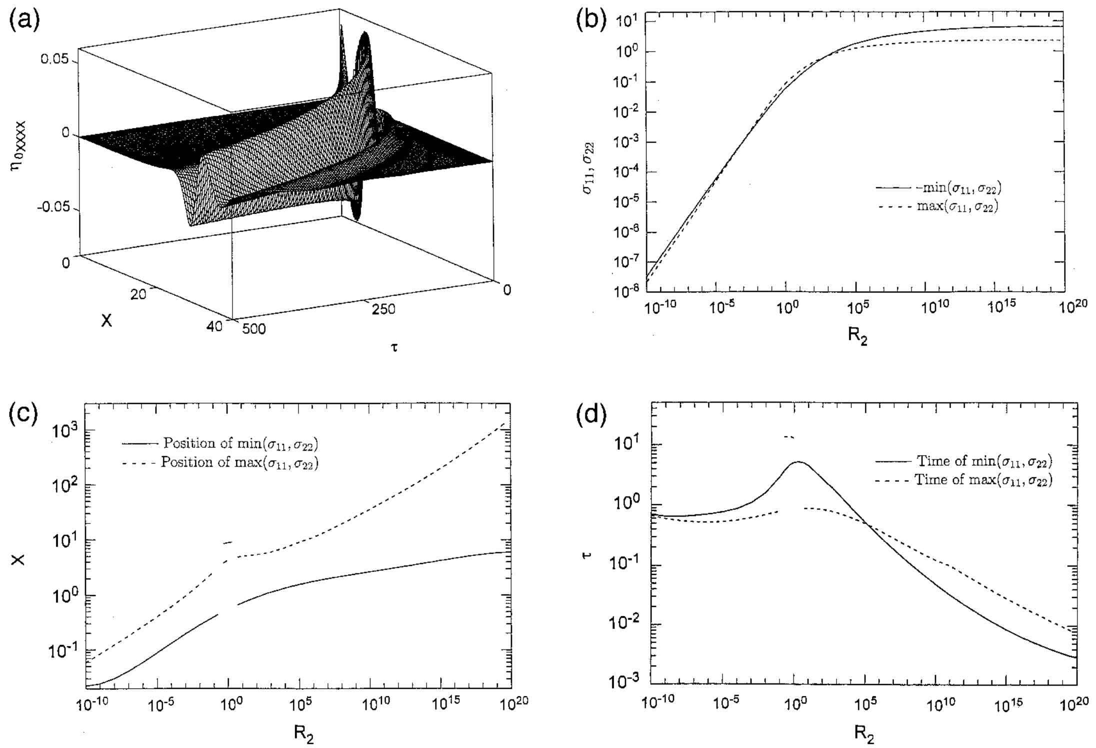

Figure 4. Plots for the leading-order normal stresses $\sigma_{11}, \sigma_{22} = -R_2\eta_{0XXXX}$ with $\kappa = 1$ in all cases. (a) is a 3-d plot of η_{0XXXX} with X and τ for the parameter value $R_2 = 1$. (b) shows the maximum and minimum value of $-R_2\eta_{0XXXX}$ with R_2, whilst (c) shows the position and (d) shows the time of these maximum and minimum values with R_2.

$d(t)$ as defined in (1.17). Interestingly, the large-time behaviour for the stresses in this limit have some noteworthy features. The stresses are largest in the region $X = O(R_2^{1/6})$ near the nitride-mask edge and are again oscillatory. These can be shown to decay for large τ, where the asymptotics are described in King [5]. Relevant to the normal stresses in the region $X = O(1)$, the implicit travelling-wave solution (1.15) and the scalings (1.13) together with (A.1) gives

$$\eta_{1XXXX} = \frac{(\gamma - 1)\kappa^2}{\gamma(\gamma f_1 + 1)^3}\left(4\log(\gamma f_1 + 1) - 3\gamma f_1\right)\,, \tag{3.5}$$

which is shown in Figure 6. The large-time behaviour of η_{1XXXX} exhibits the emergence of a travelling-wave solution, the details of which are given at the end of Appendix B. Although the normal stresses are smaller than those in $X = O(R_2^{1/6})$, they do persist at large time.

3.2.2. *Large nitride rigidity*

In the limit $R_2 \to +\infty$ for large nitride rigidity, the maximum and minimum stresses occur further under the nitride mask (Figures 4c and 5c) and at earlier times (Figures 4d and 5d). Indeed, Figure 4b suggests that the maximum normal stress tends to a limit, which is consistent with the asymptotic results described in Appendix A for this case. For large X, (A.7) gives the behaviour

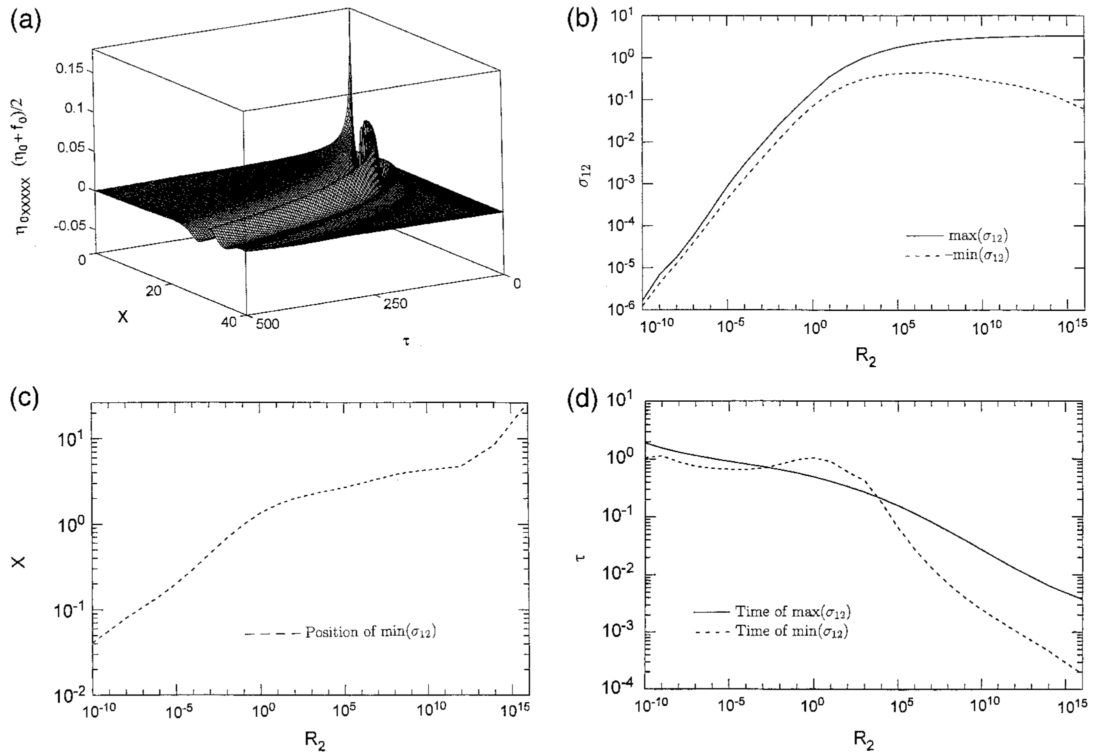

Figure 5. Plots for the leading-order tangential stress $\sigma_{12} = \epsilon R_2 \eta_{0XXXXX}(\eta_0 + f_0)/2$ on the silicon/oxide interface with $\kappa = 1$ in all cases. (a) is a 3-d plot of $\eta_{0XXXXX}(\eta_0 + f_0)/2$ with X and τ for the parameter value $R_2 = 1$. (b) shows the maximum and minimum values of σ_{12}/ϵ with R_2, whilst (c) shows the position of the minimum value with R_2 (the maximum value always occurs at $X = 0$) and (d) shows the time of the maximum and minimum values with R_2.

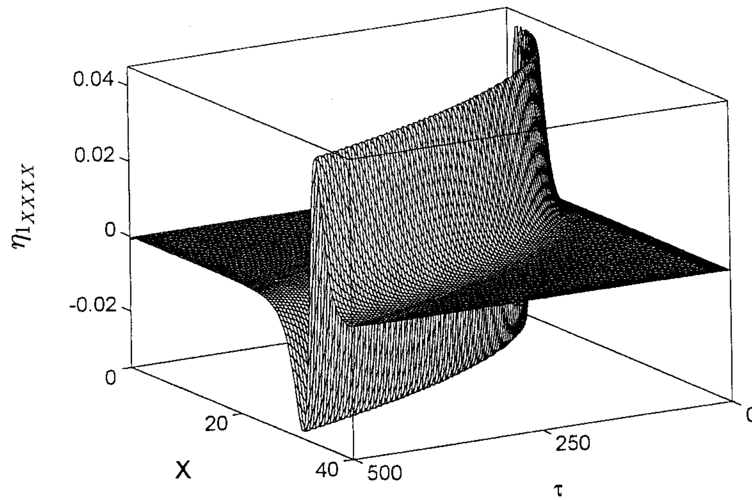

Figure 6. A 3-d plot of the fourth derivative η_{1XXXX} for the parameter values $R_2 = \kappa = 1$.

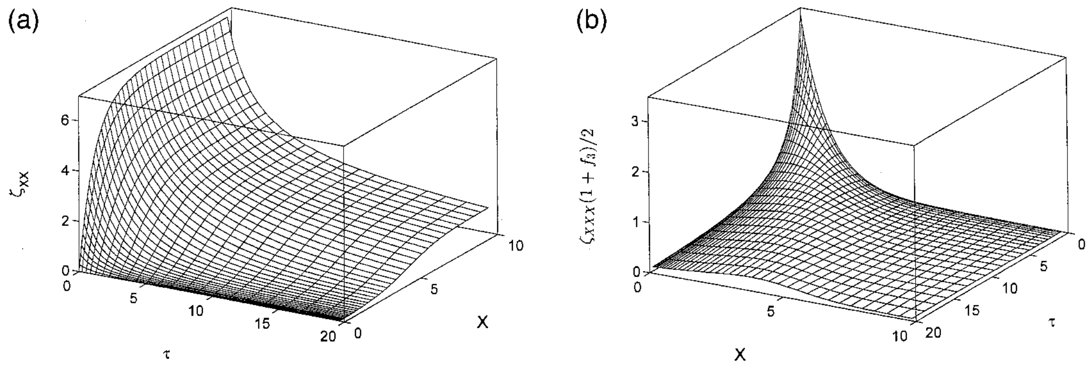

Figure 7. Plots in the large nitride rigidity case for the leading-order stresses in the region $X = O(1)$. (a) is a 3-d plot of the function ζ_{XX} whilst (b) shows the function $\zeta_{XXX}(1+f_3)/2$, both for the parameter values $R_2 = \kappa = 1$.

$$\lim_{X\to+\infty} \zeta_{XX} = \frac{12(\gamma-1)}{(2\kappa)^{1/2}}\dot{d}_3 \int_0^{\kappa\tau/\gamma} \frac{u\mathrm{d}u}{(u+1)^3\,(u-\log(1+u))^{1/2}}\,,$$

the maximum value of which occurs for small τ and is $12(\gamma-1)/\gamma \approx 6\cdot 7$ agreeing with the numerical value in Figure 4b and noting that

$$\lim_{R_2\to\infty} R_2\eta_{0XXXX} = \zeta_{XX}\,.$$

For large time, $\zeta_{XX} = O(\tau^{-1/2})$ and the normal stresses decay at this rate in both $X = O(1)$ and $X = O(R_2^{1/6})$ regions. Figure 7a illustrates the behaviour of the function ζ_{XX}. The shear stress on the oxide/silicon interface is obtained from the expression

$$\frac{(1+f_3)}{2}\zeta_{XXX} = \frac{6(\gamma-1)\dot{d}_3 f_3}{(1+f_3)^2}\,,$$

and its evolution is shown in Figure 7b.

It is in this case that the lateral extent of oxidation is the smallest, with the bird's beak length being characterised by $d_3(\tau) = d(\kappa\tau/\gamma)/\sqrt{\kappa}$ with $d(t)$ as defined in (1.17).

3.3. Finite-length masks

For finite-length masks, the system of equations governing the leading order growth of the boundaries and the stresses are now given by (1.1)–(1.3) and (1.5) with the boundary condition (1.4) replaced by the symmetry condition

$$\text{at } X = L \quad f_{0X} = 0\,, \quad \eta_{0X} = \eta_{0XXX} = \eta_{0XXXXX} = 0\,, \tag{3.6}$$

where L is the non-dimensional half length of the nitride mask (*i.e.* $L = \epsilon\ell/a$ where 2ℓ is the dimensional nitride mask length). The asymptotics for this case are significantly different from the semi-infinite mask case and are discussed in Evans *et al.* [12], although the numerical schemes in Section 2 need only minor modifications to deal with (3.6). In particular, (2.38), (2.39), (2.41) and (2.42) are now replaced by

$$g_{N,j+1} = [\eta_1]_{N,j+1} = [\eta_3]_{N,j+1} = [\eta_5]_{N,j+1} = 0, \tag{3.7}$$

which then leads to

$$\delta g_N = \delta[\eta_1]_N = \delta[\eta_3]_N = \delta[\eta_5]_N = 0. \tag{3.8}$$

As for the initial conditions, the only change is that (2.52) is replaced by

$$g_X = 0 \quad \text{at } X = L, \tag{3.9}$$

which then leads to

$$g = \frac{\kappa}{\gamma} \frac{\cosh(\sqrt{\kappa}(L - X))}{\cosh(\sqrt{\kappa} L))}, \tag{3.10}$$

and thence, for $i = 0, \ldots, N$,

$$g_{i,0} = \frac{\kappa}{\gamma} \frac{\cosh(\sqrt{\kappa}(L - X_i))}{\cosh(\sqrt{\kappa} L))}, \quad h_{i,0} = \frac{\kappa^{\frac{3}{2}}}{\gamma} \frac{\sinh(\sqrt{\kappa}(X_i - L))}{\cosh(\sqrt{\kappa} L))}. \tag{3.11–12}$$

As in the semi-infinite mask length case, the parameter κ can be scaled from the problem and thus it is sufficient to consider only the parameters R_2 and L. Figures 8a and 8b describe the variation of the maximum and minimum values of the normal stress $R_2 \eta_{0_{XXXX}}$ with both R_2 and L, whilst Figures 8c and 8d describe the variation of the maximum and minimum values of the tangential stress (scaled with ϵ) $R_2 \eta_{0_{XXXXX}}(\eta_0 + f_0)/2$ with both R_2 and L. In each case, the maximum and minimum values are the same order of magnitude for each L and show the same qualitative behaviour as for the infinite length mask, *i.e.* their position being progressively further under the nitride mask (up until the symmetry boundary $X = L$) and occurring at earlier times as the rigidity coefficient increases.

From the results in Section 3.1 for L infinite, the large-time approximation holds for $t \geq O(t_1 = 50)$, the moving parabola forming a significant part of the approximation when $t \geq O(t_2 = 1000)$, and the scalings (1.13) and (1.14) with $\kappa = 1$ giving the the corresponding times for small nitride rigidities ($R_2 \ll 1$) and for large nitride rigidities ($R_2 \gg 1$), respectively. Thus we would expect to see these large-time approximations in the L infinite case, form solutions for intermediate-time in the L finite case when $L \geq \sqrt{2t_1} \approx 15$, with $L \geq \sqrt{2t_2} \approx 45$ for a near parabolic interface shape. Figure 9 shows the growth of the oxide thickness $(\eta_0(L, \tau) + f_0(L, \tau))$ at the mask mid-point $X = L$ for varying R_2 and L with $\kappa = 1$. The larger values of L show that the approximations of $L^2/2$ for large rigidity and $\gamma L^2/2$ for small rigidity, obtained from the the moving-parabola solution, are reasonable indications of the times at which the lateral extent of oxidation reach the symmetry boundary.

4. Application of results

Here we provide values for the dimensional model parameters, in order to ascertain which part of the physical parameter space the reaction-controlled limit is valid. The results obtained in previous sections are also scaled to give dimensional values which are more relevant to process engineers and other practitioners.

Some of these dimensional parameters show a wide range of values that vary with different process conditions. For instance, the diffusion coefficient D is affected by temperature, oxidising ambient (dry O_2 or wet H_2O) and the external pressure of the oxidising ambient,

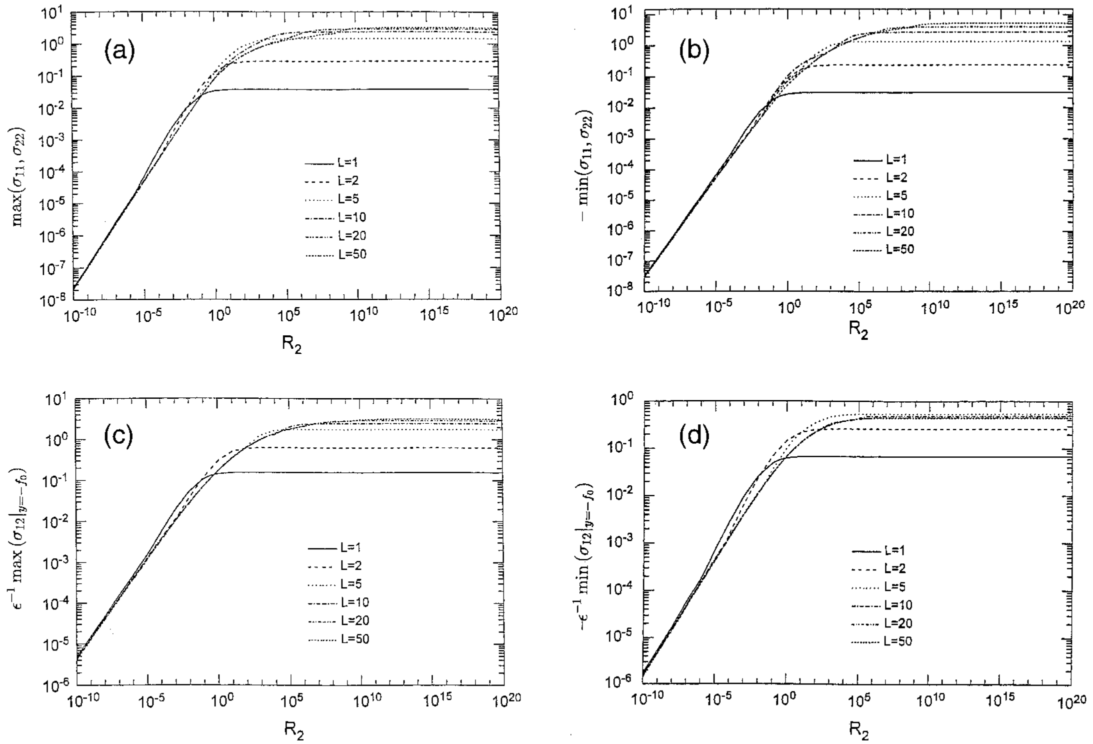

Figure 8. Plots in the finite-mask length case for the leading-order normal stresses $\sigma_{11} = \sigma_{22} = -R_2\eta_{0XXXX}$ and tangential stress $\sigma_{12} = -\epsilon R_2\eta_{0XXXXX}(\eta_0 + f_0)/2$ with $\kappa = 1$. (a) shows the maximum values of $R_2\eta_{0XXXX}$ with R_2 for selected values of L, whilst (b) shows the minimum values with R_2 for the same values of L. (c) illustrates the maximum values of $R_2\eta_{0XXXXX}(\eta_0 + f_0)/2$ with R_2 for selected values of L, whilst (d) shows the minimum values with R_2 for the same values of L.

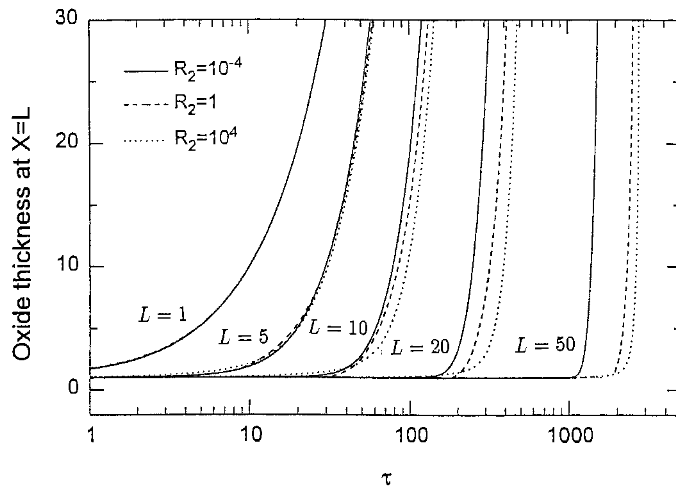

Figure 9. The growth of the oxide thickness at $X = L$ (the centre position of the mask), *i.e.* $f_0(L, \tau) + \eta_0(L, \tau)$ for varying mask lengths $L = 1, 5, 10, 20, 50$ with for each L the values of the rigidity coefficient $R_2 = 10^{-4}$ (small), 1 (intermediate) and 10^4 (large).

Table 1. Dimensional parameter values for selected temperatures and wet/dry oxidation conditions (SI Units: 1 Pa = 1 N/m^2 = 10 dyne cm^{-2}; 1 poise = 10^{-1} Pa s)

T(°C)	Ambient	D (cm^2/s)	K (cm/s)	c^* (cm^{-3})	N (cm^{-3})	μ (poise)
1200	Dry	$2{\cdot}70 \times 10^{-8}$	$1{\cdot}35 \times 10^{-2}$	$5{\cdot}2 \times 10^{16}$	2.25×10^{22}	
1100	Dry	$1{\cdot}43 \times 10^{-8}$	$3{\cdot}61 \times 10^{-3}$	$5{\cdot}2 \times 10^{16}$	$2{\cdot}25 \times 10^{22}$	
1000	Dry	$6{\cdot}58 \times 10^{-9}$	$8{\cdot}53 \times 10^{-4}$	$5{\cdot}2 \times 10^{16}$	$2{\cdot}25 \times 10^{22}$	
900	Dry	$2{\cdot}65 \times 10^{-9}$	$2{\cdot}07 \times 10^{-4}$	$5{\cdot}2 \times 10^{16}$	$2{\cdot}25 \times 10^{22}$	
800	Dry	$9{\cdot}00 \times 10^{-10}$	$3{\cdot}61 \times 10^{-5}$	$5{\cdot}2 \times 10^{16}$	$2{\cdot}25 \times 10^{22}$	
1200	Wet	$1{\cdot}5 \times 10^{-9}$	$6{\cdot}0 \times 10^{-4}$	$3{\cdot}0 \times 10^{19}$	$4{\cdot}50 \times 10^{22}$	$6{\cdot}0 \times 10^{11}$
1100	Wet	$1{\cdot}22 \times 10^{-9}$	$1{\cdot}94 \times 10^{-4}$	$3{\cdot}0 \times 10^{19}$	$4{\cdot}50 \times 10^{22}$	$6{\cdot}0 \times 10^{12}$
1000	Wet	$7{\cdot}21 \times 10^{-10}$	$5{\cdot}30 \times 10^{-5}$	$3{\cdot}0 \times 10^{19}$	$4{\cdot}50 \times 10^{22}$	$3{\cdot}0 \times 10^{13}$
900	Wet	$3{\cdot}89 \times 10^{-10}$	$1{\cdot}16 \times 10^{-5}$	$3{\cdot}0 \times 10^{19}$	$4{\cdot}50 \times 10^{22}$	$3{\cdot}0 \times 10^{14}$
800	Wet	$1{\cdot}87 \times 10^{-10}$	$1{\cdot}89 \times 10^{-6}$	$3{\cdot}0 \times 10^{19}$	$4{\cdot}50 \times 10^{22}$	$1{\cdot}0 \times 10^{15}$

whilst the reaction coefficient K, in addition, is affected by the crystal orientation of the silicon substrate and doping concentrations. The equilibrium concentration of oxidant in the oxide c^* is dependent on the oxidising ambient and the external pressure, and the viscosity of the oxide μ is temperature dependent. These variations are discussed in Deal and Grove [6], Powell *et al.* [13], Hess and Deal [14], Sze [15], Hu [16], Massoud *et al.* [17, 18], Camelin *et al.* [19], Irene and Ghez [20], Kao *et al.* [21], Lewis and Irene [22], Irene [23], Katz [24], Umimoto *et al.* [25], Susa and Nagata [27]. Table 1 provides a range of values for these particular dimensional parameters, which were taken from Deal and Grove [6], EerNisse [28], Chin *et al.* [29] and Wilson and Marcus [30].

Thin initial pad oxide thicknesses a are usually upto 1000 Å (with those less than 50 Å being termed ultra-thin), whilst nitride mask thicknesses, d, are typically in the range 100 Å–5000 Å, see for example Bassous and Maniscalco [31], Bohg and Gaind [32], Magdo and Bohg [33], Isomae *et al.* [34], Shibata and Taniguchi [35], Tamaki *et al.* [36, 37], Chin *et al.* [29], Isomae [10], Poncet [8], Tung and Antoniadis [38], Singh *et al.* [39], Chiou *et al.* [40], Huang and Jaccodine [41], Umimoto and Odanaka [42]. Typical mask lengths ℓ can be anywhere in the range $0{\cdot}3\mu$m–10 μm, with the smaller values being more common recently as packing densities have increased (Kenkare *et al.* [43] and Park *et al.* [44]).

For the nitride mask, a Young's Modulus $E = 3 \times 10^{11}$ Pa and a Poisson's Ratio $\nu = 0{\cdot}3$ are typical and are taken from Irene *et al.* [45]. Values of similar magnitude can be found in Poncet [8], Isomae and Yamamoto [11], Umimoto and Odanaka [42]. The inertia of the nitride mask I Å^3 is given by $I = d^3/12(1 - \nu^2)$ (Umimoto and Odanaka [42]).

We now consider the applicability of the reaction rate limit and the determination of the dimensionless parameters. Importantly we remark that the original model assumes the oxide to be an incompressible Newtonian viscous fluid, which is reasonable for process temperatures above 965^oC (EerNisse [28, 46], Tan and Gösele [47], Irene *et al.* [45] and Tiller [48]). For lower temperatures a viscoelastic or even elastic oxide should be considered. The diffusion of oxidant was also assumed to be in quasi-steady state and is a reasonable assumption if $\lambda \gg 1$ which is supported by its calculated values in Table 2. For the reaction-controlled limit we require that the initial pad oxide thickness $a \ll D/K$, where D/K is a representative

Table 2. Important dimensional parameter combinations calculated from the values in Table 1, using also $E = 3 \times 10^{11}$ Pa and $\nu = 0.3$ for the nitride mask

T (°C)	Ambient	D/K (Å)	λ	$\lambda D/K^2$	$\frac{\mu D}{\lambda}$ (Pa Å^2)	$\frac{\lambda E}{12\mu D(1-\nu^2)}$ (Å^{-2})
1200	Dry	200	$1{\cdot}92 \times 10^5$	28 s		
1100	Dry	396	$1{\cdot}92 \times 10^5$	3 min 31 s		
1000	Dry	771	$1{\cdot}92 \times 10^5$	29 min		
900	Dry	1280	$1{\cdot}92 \times 10^5$	3 hr 18 min		
800	Dry	2493	$1{\cdot}92 \times 10^5$	36 hr 50 min		
1200	Wet	250	$6{\cdot}67 \times 10^2$	3 s	$1{\cdot}35 \times 10^{15}$	$2{\cdot}04 \times 10^{-5}$
1100	Wet	629	$6{\cdot}67 \times 10^2$	22 s	$1{\cdot}10 \times 10^{16}$	$2{\cdot}50 \times 10^{-6}$
1000	Wet	1360	$6{\cdot}67 \times 10^2$	2 min 51 s	$3{\cdot}24 \times 10^{16}$	$8{\cdot}49 \times 10^{-7}$
900	Wet	3353	$6{\cdot}67 \times 10^2$	32 min 8 s	$1{\cdot}75 \times 10^{17}$	$1{\cdot}57 \times 10^{-7}$
800	Wet	9894	$6{\cdot}67 \times 10^2$	9 hr 42 min	$2{\cdot}80 \times 10^{17}$	$9{\cdot}82 \times 10^{-8}$

oxidation length (values for which are shown in Table 2). This limit is physically relevant and has been considered by Shibata and Taniguchi [35] and Wu *et al.* [49]. The dimensionless parameters $\{\epsilon, \kappa, R_2, L\}$ are determined by the following relationships

$$\epsilon^2\kappa = \frac{K}{D}a \,, \quad R_2\epsilon^{-4} = \frac{\lambda E}{12\mu D(1-\nu^2)}\frac{d^3}{a} \,, \quad L = \epsilon\frac{\ell}{a} \,, \tag{4.1}$$

and the dimensional time scale $\bar{t}$ and the dimensional stresses $\bar{\sigma}_{ij}$ are given by

$$\bar{t} = \frac{\lambda a^2}{D\epsilon^2}\tau \,, \quad \bar{\sigma}_{ij} = \frac{\mu D}{\lambda a^2}\sigma_{ij} \,, \tag{4.2}$$

where τ is the dimensionless time scale and σ_{ij} are dimensionless stresses.

Denoting the dimensional field oxide thickness by $\bar{x}_0 = \bar{f} + \bar{h} = \gamma\bar{f} + a$ cm, then the one-dimensional solution (1.6), when written in dimensional terms, becomes

$$\bar{x}_0^2 + A^*\bar{x}_0 = B^*\left(\bar{t} + \bar{t}_0\right)$$

where $A^* = 2D\left(\frac{1}{\bar{H}} + \frac{1}{K}\right)$, $B^* = 2Dc^*\gamma/N$ termed the parabolic rate constant and $\bar{t}_0 = (a^2 + A^*a)/B^*$. It is worth remarking that since the gas/oxide transport coefficient $\bar{H} \gg K$ ($\bar{H} = O(2{\cdot}8$ cm/s)), then the characteristic length $D/K \approx A^*/2$ where A^* is a well-investigated rate constant in the Deal-Grove one-dimensional oxidation model (Deal and Grove [6]). As remarked by Marcus and Sheng [50] and as we note from Table 2, the characteristic length D/K for the oxidation process decreases as the temperature increases. This characteristic length represents the transition thickness at which the field oxide oxidation kinetics (which are the one-dimensional Deal-Grove solution) change from linear to parabolic. Thus at lower temperatures the linear rate law dominates for more extensive oxidation times and the reaction-controlled limit is valid for larger pad oxide thicknesses. As remarked in Section 1, the reaction-controlled limit holds until $\tau = O(\epsilon^{-2})$ which in dimensional terms

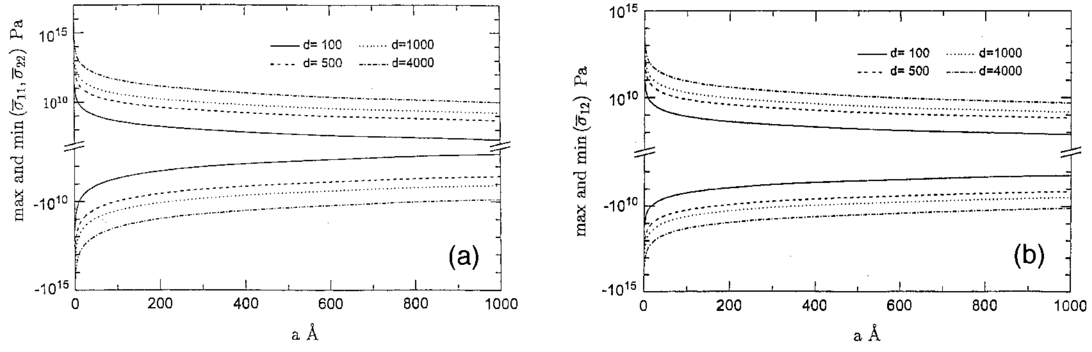

Figure 10. Plots of the variation of the dimensional stresses at $T = 1000°C$ with varying pad oxide a and nitride mask d thicknesses. (a) shows the maximum normal stress $(\max\{\bar{\sigma}_{11}, \bar{\sigma}_{22}\})$, (b) the minimum normal stress $(\min\{\bar{\sigma}_{12}, \bar{\sigma}_{22}\})$, (c) the maximum tangential stress $(\max\{\bar{\sigma}_{12}\})$ and (d) the minimum tangential stress $(\min\{\bar{\sigma}_{12}\})$.

is $O(\lambda D/K^2)$ s. This represents the characteristic time of the oxidation process and agrees with the value $O(A^{*2}/4B^*)$ in the Deal-Grove model which marks the time corresponding to the transition of linear to parabolic growth regimes. Experimentally the smallest pad oxide values that can be obtained are around 2 Å (Morita and Ohmi [51]), which gives $O(10^{-4})$ as the realistic smallest value of ϵ that may be obtained.

The criteria for choosing the model with a semi-infinite length mask, or that with a finite length, depends upon the relative sizes of the dimensional length l and the characteristic distance of the oxidation process D/K. If $\ell \leq O(D/K)$ then a finite-length mask would be applicable, otherwise a semi-infinite length mask should be considered. This follows since the reaction-controlled stage lasts until $\tau = O(\epsilon^{-2})$ and we would expect the lateral extent of the oxidation to be at most $O(\epsilon^{-1})$ using the moving parabola solution for the large-time behaviour of the silicon/oxide interface. Thus if $L \geq O(\epsilon^{-1})$ then the tip of the moving-parabola solution $(2\tau)^{1/2}$ will not reach the symmetry boundary $X = L$ by the end of oxidation time for which the reaction-controlled limit is valid.

Figure 10 illustrates the behaviour of the maximum and minimum stresses with varying pad oxide and nitride thicknesses for oxidation in a wet ambient at a chosen representative temperature of 1000 °C. The values in Tables 1 and 2 have been used, as well as the results for the maximum non-dimensional stresses discussed in Section 3.2 and the scalings,

$$R_2 = \beta_1 a d^3 , \quad (\bar{\sigma}_{11}, \bar{\sigma}_{22}) = \frac{\beta_2}{a^2}(\sigma_{11}, \sigma_{22}) \quad \bar{\sigma}_{12} = \frac{\beta_3}{a^{3/2}}(\sigma_{12}/\epsilon) , \tag{4.3}$$

which show the dependence of the dimensional stresses on the pad oxide and nitride thicknesses, where

$$\beta_1 = \frac{\lambda E}{12\mu D(1-\nu^2)}\left(\frac{K}{D}\right)^2 , \quad \beta_2 = \frac{\mu D}{\lambda} , \quad \beta_3 = \frac{\mu D}{\lambda}\left(\frac{K}{D}\right)^{1/2} ,$$

are coefficients, the values of which change with temperature (Table 2). We remark that without loss of generality we have taken $\kappa = 1$ so that $\epsilon = (Ka/D)^{1/2}$. The maximum stresses increase as the nitride thickness increases and/or the pad oxide thickness decreases, thus increasing the chance of dislocation onset. This agrees well with the experimental findings of Bohg and Gaind [32], Magdo and Bohg [33], Shibata and Taniguchi [35], Tamaki *et al.* [36, 37], Isomae [10] and Huang and Jaccodine [41]. The stress field in the silicon substrate

may produce defects if its value (generally a resolved component of the normal and/or shear stress in a critical direction depending on the silicon orientation, see for example Isomae [10], Isomae and Yamamoto [11]) is above the yield threshold determined experimentally by Tamura and Sunami [9], Vanhellemont and Claeys [52] to be in the range $0{\cdot}7 \times 10^7$ to $4{\cdot}9 \times 10^7$ Pa. (This assumes that the starting material is defect-free and that dislocations are nucleated, the stress threshold for which is much larger than that required to cause glide of already existing defects.) Although the values in Figure 10 are slightly higher than this figure, the resolved components can be one or two orders of magnitude less, varying also with the orientation of the silicon substrate. The position of the maximum stresses are seen from Figures 5c and 6c to be close to the nitride edge which is where disslocation onset is most likely to occur, also agreeing with the experimental results of the aforementioned authors. Finally it should be noted that the scaling (4.3) for the stress agrees in its order of magnitude with that reported in Matsumoto and Fukuma [53] and Isomae [54].

5. Discussion

Numerical finite-difference schemes have been presented in Section 2 for two important systems of partial differential equations which arise out of the asymptotic analysis of the reaction-controlled oxidation case. These partial differential equations are central in describing the leading-order growth of the oxide boundaries under the nitride mask and the main stresses that occur within the oxide.

An interesting feature of the stresses are their oscillatory behaviour, which qualitatively agree with the numerical results of other (similar) models used by Chin *et al.* [29], Matsumoto and Fukuma [53], Tung and Antoniadis [38], Isomae [54] and Isomae and Yamamoto [11]. This is particularly important in deciding on the appropriate functional form to use of a stress-dependent reaction coefficient and diffusion coefficient, which have recently been introduced to account for the importance of stress effects during the oxidation process (Kao *et al.* [21], Sutardja and Oldham [56] and Umimoto *et al.* [26]). The stress oscillations are confined to the mask edge for small nitride rigidities and the central mask region for large nitride rigidities, that is, the oscillations are pushed to the extremities of the semi-infinite mask for the large and small mask rigidities.

The reaction-controlled oxidation limit, corresponding to small initial pad oxide thicknesses (relative to the characteristic oxidation length D/K), is a particular parameter limit which allows analytical progress in the whole oxide region for the local oxidation of silicon (LOCOS) process. It is this limit which is of interest practically since it reduces the extent of lateral oxidation under the nitride mask (bird's beak encroachment). Unfortunately, associated with small pad oxide thicknesses are large oxide stresses which can cause dislocation onset with detrimental results on subsequent device isolation and operation. These associated stress fields and the degree of lateral oxidation encroachment have been investigated in this paper with good quantitative agreement with experimental observations. The dimensional results in Section 4 for the maximum and minimum oxidation-induced stresses demonstrate how their values can change by several orders of magnitude when the pad-oxide and nitride-mask thicknesses are varied within experimental ranges. In practice, it is the resolved components of stress that are of interest; these may be determined by use of (1.8) together with dimensional scalings (4.2) and then compared to critical yield stress values in order to indicate when dislocation onset is likely in the silicon substrate. This information together with the analytical

expressions (particularly the moving parabola solutions at large time) for estimation of the bird's beak length, provide important information about the underlying oxidation process in the LOCOS geometry.

Appendix A

(1) *Small nitride rigidity.* To consider the limit $R_2 \to 0$ we pose the expansions

$$f_0 \sim f_1 + O(R_2) , \qquad \eta_0 \sim \eta_1 + O(R_2) ,$$

in $X = O(1)$ for which (1.1)–(1.5) yields

$$\eta_1 = (\gamma - 1) f_1 + 1 , \tag{A.1}$$

and

$$\left.\begin{array}{ll} & \kappa f_{1_\tau} = \left((\gamma f_1 + 1) f_{1_{X\tau}}\right)_X , \\ \text{at } X = 0: & f_1 = \dfrac{\kappa}{\gamma}\tau , \\ \text{as } X \to \infty: & f_1 \to 0 , \\ \text{at } \tau = 0: & f_1 = 0 , \end{array}\right\} \tag{A.2}$$

for the leading-order problem for the growth of the interfaces. This solution does not satisfy the boundary conditions for η_0 at $X = 0$ in (1.3) and we find that a boundary layer is required near $X = 0$, the scaling for which is $X = R_2^{1/6}\chi$. In $\chi = O(1)$ we obtain the expansions (after matching with the region $X = O(1)$)

$$f_0 \sim \frac{\kappa\tau}{\gamma} + R_2^{1/6}\chi f_{1_X}(0,\tau) + R_2^{1/3}\frac{1}{2}\chi^2 f_{1_{XX}}(0,\tau) ,$$

$$\eta_0 \sim 1 + \frac{(\gamma-1)}{\gamma}\kappa\tau + R_2^{1/6}(\gamma-1)\chi f_{1_X}(0,\tau) + R_2^{1/3}\eta_1^* ,$$

where η_1^* is given by

$$\eta_1^* = (\gamma-1)\frac{\chi^2}{2}\frac{\kappa^2\tau}{\gamma(1+\kappa\tau)} + N ,$$

and N satisfies the problem,

$$\left.\begin{array}{ll} & N_\tau = \frac{1}{12}(1+\kappa\tau)^3 N_{\chi\chi\chi\chi\chi\chi} , \\ \text{at } \chi = 0: & N_{\chi\chi} = -\dfrac{(\gamma-1)\kappa^2\tau}{\gamma(1+\kappa\tau)} , N_{\chi\chi\chi} = N_{\chi\chi\chi\chi} = 0 , \\ \text{as } \chi \to +\infty: & N \to 0 , \\ \text{at } \tau = 0: & N = 0 . \end{array}\right\} \tag{A.3}$$

The leading-order stresses in this case are

$$X = O(R_2^{1/6}): \quad \sigma_{11}, \sigma_{22} \sim -R_2^{2/3} N_{XXXX},$$

$$\sigma_{12} \sim \epsilon R_2^{1/2} N_{XXXXX} \left(-y + \frac{1}{2} \left(1 + (\gamma - 1) \frac{\kappa \tau}{\gamma} \right) \right);$$

$$X = O(1): \quad \sigma_{11}, \sigma_{22} \sim -R_2 \eta_{1_{XXXX}},$$

$$\sigma_{12} \sim \epsilon R_2 \eta_{0_{XXXXX}} \left(-y + \frac{1}{2} (\eta_1 - f_1) \right) \tag{A.4}$$

which are now much smaller with the largest occurring in the region $X = O(R_2^{1/6})$ near the nitride mask edge.

(2) *Large nitride rigidity.* In the limit $R_2 \to \infty$, we seek expansions in the form

$$f_0 \sim f_3 + o(1), \quad \eta_0 \sim \eta_3 + o(1), \quad \eta_{0_{XX}} \sim \frac{1}{R_2} \zeta,$$

where at leading order the nitride is regarded as rigid, $\eta_3 \equiv 1$. We obtain

$$\left.\begin{aligned} & \kappa f_{3_\tau} = \left((1 + f_3) f_{3_{X\tau}} \right)_X, \\ \text{at } X = 0: \quad & f_3 = \frac{\kappa}{\gamma} \tau, \\ \text{at } X \to +\infty: \quad & f_3 \to 0, \\ \text{at } \tau = 0: \quad & f_3 = 0, \end{aligned}\right\} \tag{A.5}$$

together with

$$\left.\begin{aligned} & -(\gamma - 1) f_{3_\tau} = \tfrac{1}{12} \left((1 + f_3)^3 \zeta_{XXX} \right)_X, \\ \text{at } X = 0: \quad & \zeta = \zeta_X = \zeta_{XX} = 0, \\ \text{as } X \to +\infty: \quad & \zeta_{XXX} \to 0. \end{aligned}\right\} \tag{A.6}$$

Using the travelling wave solution (1.15) with the scalings (1.14) as the solution to (A.5), we may integrate (A.6) to give

$$\zeta_{XX} = \frac{12(\gamma - 1)\dot{d}_3}{(2\kappa)^{1/2}} \int_{f_3}^{\kappa\tau/\gamma} \frac{u \,\mathrm{d}u}{(u + 1)^3 (u - \log(1 + u))^{1/2}}, \tag{A.7}$$

with

$$\dot{d}_3 = \left(\frac{\kappa}{2} \right)^{1/2} \frac{1}{\gamma \left(\frac{\kappa \tau}{\gamma} - \log \left(1 + \frac{\kappa \tau}{\gamma} \right) \right)^{1/2}}.$$

An additional region is required since (A.7) does not satisfy $\zeta_{XX} \to 0$ as $X \to \infty$, the scaling for which is $X = R_2^{1/6} \chi$. In $\chi = O(1)$, f_0 can be shown to be exponentially small, and thus we have

$$\eta_0 \sim 1 + R_2^{-1/3} \eta_3^*,$$

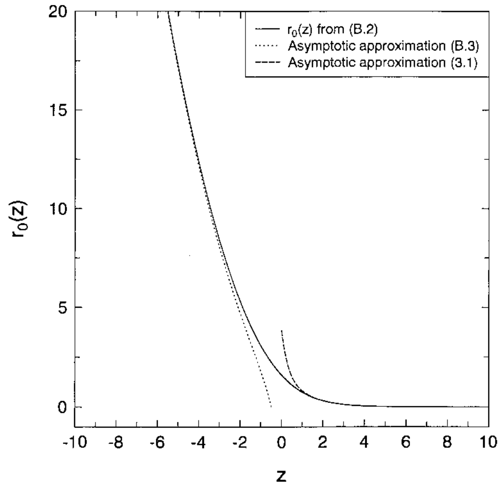

Figure 11. Plot of the inner solution r_0 from (B.2) and the asymptotic approximations (B.3) and (3.1) with $a_0 = 2{\cdot}553$.

with

$$\left.\begin{aligned} &\eta^*_{3_\tau} = \tfrac{1}{12}\eta^*_{3_{XXXXXX}} , \\ &\text{at } \chi = 0: \quad \eta^*_{3_{XX}} = \eta^*_{3_{XXX}} = 0 , \quad \eta^*_{3_{XXXX}} = \lim_{X\to\infty} \zeta_{XX} , \\ &\text{as } \chi \to +\infty: \ \eta^*_3 \to 0 , \\ &\text{at } \tau = 0: \quad \eta^*_3 = 0 . \end{aligned}\right\} \tag{A.8}$$

The leading-order stresses in this case are

$$\left.\begin{aligned} X = O(1) \quad & \sigma_{11}, \sigma_{22} \sim -\zeta_{XX} , \\ & \sigma_{12} \sim \epsilon \zeta_{XXX}\left(-y + \tfrac{1}{2}(1 - f_3)\right) ; \\ X = O(R_2^{1/6}) , \quad & \sigma_{11}, \sigma_{22} \sim -\eta^*_{3_{XXXX}} , \\ & \sigma_{12} \sim \epsilon R_2^{-1/6} \eta^*_{3_{XXXXX}}\left(-y + \tfrac{1}{2}\right) , \end{aligned}\right\} \tag{A.9}$$

with the largest stresses occurring in both the $X = O(1)$ and $\chi = O(1)$ regions far under the nitride mask.

These results are analagous to those derived in King [5], albeit by a slightly different method, and are recovered by setting $R_2 = \epsilon^2 R_1$ for small nitride rigidity and $R_2 = \epsilon^{-3} R_3$ for large nitride rigidity with $R_1, R_3 = O(1)$.

Appendix B

To describe the large-time behaviour of (1.19)–(1.12), we introduce the scalings

$$T = \theta t , \quad F = \theta f , \quad Y = \theta^{1/2} x ,$$

using an artificial small parameter θ, and consider the limit $\theta \to 0$. We obtain the following structure:

(a) An outer region $0 < Y < \sqrt{2T}$ in which $F \sim F_0 + o(\theta^{1/2})$ with the self-similar solution

$$F_0 = TG(\xi) , \quad \xi = \frac{Y}{\sqrt{2T}} , \tag{B.1}$$

where

$$G(\xi) = \begin{cases} (1-\xi)^2 , & \xi < 1 , \\ 0 , & \xi > 1 . \end{cases}$$

(b) An inner region with $F = \theta(r_0(z) + o(1))$ and $Y = \sqrt{2T} + \theta^{1/2} z$, so that in $z = O(1)$ we have

$$\sqrt{2} z = \int_{r_0}^{a_2} \frac{\mathrm{d}u}{(u - \log(1+u))^{1/2}} \tag{B.2}$$

where a_2 is a constant which is determined by the matching condition

$$r_0 \sim \frac{z^2}{2} + 2\log(-z) - \log 2 + 2 + o(1) , \quad \text{as } z \to -\infty . \tag{B.3}$$

Figure 11 indicates that this is a good approximation for $z < -5$ and numerically we obtain $a_2 = 1{\cdot}607$. The outer moving parabola solution (B.1) is thus expected to hold for $Y < \sqrt{2T} - 5\theta^{1/2}$ or equivalently for $x < \sqrt{2t} - 5$. As $z \to +\infty$, the asymptotic behaviour of r_0 is exponential and is given by (3.1) where now $a_0 = 2{\cdot}553$.

(c) In the third region $\sqrt{2T} < Y$, f is exponentially small and has the form,

$$f \sim a_0 e^{(\sqrt{2T} - Y)/\theta^{1/2}} .$$

Relevant to the stresses in the small rigidity case ($R_2 \to 0$) in $X = O(1)$, we note that f_{xxxx} is $o(\theta^{3/2})$ in the outer region, exponentially small in the third region, and in the inner region is $O(1)$ and has the form

$$f_{xxxx} \sim r_{0_{zzzz}} = \frac{1}{(1+r_0)^3} (4\log(1+r_0) - 3r_0) .$$

Thus for large time, using the transformation (1.13), we have that

$$\eta_{0XXXX} \sim \frac{(\gamma - 1)\kappa^2}{\gamma(1+r_0)^3} (4\log(1+r_0) - 3r_0) ,$$

which is of $O(1)$ in magnitude in a region of length $O(1)$ around the moving tip $X = \sqrt{2\tau}$. Formally, in the large time variables Y and T, it should be noted this corresponds to a moving dipole where $F_{YYYY} = -\delta'\left(Y - \sqrt{2T}\right)$ and $\delta'(\cdot)$ denotes the derivative of the generalised delta function. Curiously then, a residual stress field seems to persist at large time in the small nitride rigidity case.

References

1. J. A. Appels, E. Kooi, M. M. Paffen, J. J. H. Schatorjé and W. H. C. G. Verkuylen, Local oxidation of silicon and its application in semiconductor-device technology. *Philips Res. Rep.* 25 (1970) 118–132.

2. J. R. King, *Mathematical Aspects of Semiconductor Process Modelling.* D. Phil. Thesis, Oxford University (1986) 408pp.
3. J. R. King, The isolation oxidation of silicon. *SIAM J. Appl. Math.* 49 (1989) 264–280.
4. A. B. Tayler and J. R. King, Free boundaries in semi-conductor fabrication. In, *Free boundary problems: theory and applications*, K.H. Hoffman and J. Sprekels, Volume I, Pitman research notes in mathematics series, Longman Sci. and Tech. (1990) 243–259.
5. J. R. King, The isolation oxidation of silicon - the reaction-controlled case. *SIAM J. Appl. Math.* 49 (1989) 1064–1080.
6. B. E. Deal and A. S. Grove, General relationship for the thermal oxidation of silicon. *J. Appl. Phys.* 36 (1965) 3770–3778.
7. T. Cebeci and P. Bradshaw, *Momentum Transfer in Boundary Layers*. Washington: Hemisphere Publishing Corporation (1977) 391pp.
8. A. Poncet, Finite-element simulation of local oxidation of silicon. *IEEE Trans. Computer-Aided Design CAD*-4 (1985) 41–53.
9. M. Tamura and H. Sunami, Generation of dislocations induced by chemical vapor deposited Si_3N_4 films on silicon. *Jpn. J. Appl. Phys.* 11 (1972) 1097–1105.
10. S. Isomae, Stress in silicon at Si_3N_4/SiO_2 film edges and viscoelastic behaviour of SiO_2 films. *J. Appl. Phys.* 57 (1985) 216–223.
11. S. Isomae and S. Yamamoto, A new two-dimensional silicon oxidation model. *IEEE Trans. CAD.* 6 (1987) 410–416.
12. J. D. Evans, J. R. King and A. B. Tayler, Finite length mask effects in the isolation oxidation of silicon. *IMA J. Appl. Math.* (1997) 58 121–146.
13. R. J. Powell, J. R. Ligenza and M. S. Schneider, Selective oxidation of silicon in low-temperature high-pressure steam'. *IEEE Trans. Electron Dev. ED*-21 (1974) 636–640.
14. D. W. Hess and B. E. Deal, Kinetics of the thermal oxidation of silicon in O_2/HCl mixtures. *J. Electrochem. Soc.* 124 (1977) 735–739.
15. S. M. Sze (ed.), *VLSI Technology*. New York: McGraw-Hill (1988) 654pp.
16. S. M. Hu, Thermal oxidation of silicon: Chemisorption and linear rate constant. *J. Appl. Phys.* 55 (1984) 4095–4105.
17. H. Z. Massoud, J. D. Plummer and E. A. Irene, Thermal Oxidation of Silicon in Dry Oxygen Growth-Rate Enhancement in the Thin Regime. I. Experimental Results. *J. Electrochem. Soc.* 132 (1985) 2685–2693.
18. H. Z. Massoud, J. D. Plummer and E. A. Irene, Thermal Oxidation of Silicon in Dry Oxygen Growth-Rate Enhancement in the Thin Regime. II. Physical Mechanisms. *J. Electrochem. Soc.* 132 (1985) 2693–2700.
19. C. Camelin, G. Demazeau, A. Straboni and J. L. Buevoz, High pressure dry oxidation kinetics of silicon - evidence of a highly stressed SiO_2 structure. *Appl. Phys. Lett.* 48 (1986) 1211–1213.
20. E. A. Irene and R. Ghez, Thermal oxidation of silicon: New experimental results and models. *Appl. Surf. Sci.* 30 (1987) 1–16.
21. D.-B. Kao, J. P. McVittie, W. D. Nix and K. C. Saraswat, Two-dimensional thermal oxidation of silicon–I. Experiments. *IEEE Trans. Electron Dev. ED*-34 (1987) 1008–1017.
22. E. A. Lewis and E. A. Irene, The Effect of Surface Orientation on Silicon Oxidation Kinetics. *J. Electrochem. Soc.* 134 (1987) 2332–2339.
23. E. A. Irene, Models for the oxidation of silicon. *CRC Critical Reviews in Solid State and Materials Sciences* 14 (1988) 175–223.
24. L. E. Katz, Oxidation. In: S. M. Sze (ed.) *VLSI Technology.* 2nd Edition, New York: McGraw-Hill (1988) 98–140.
25. H. Umimoto, S. Odanaka and I. Nakao, Numerical simulation of stress-dependent oxide growth at convex and concave corners of trench structures. *IEEE Electron Dev. Lett.* 10 (1989) 330–332.
26. H. Umimoto, S. Odanaka, I. Nakao and H. Esaki, Numerical modeling of nonplanar oxidation coupled with stress effects. *IEEE Trans. Computer-Aided Design* 8 (1989) 599–607.
27. M. Susa and K. Nagata, Thermal oxidation of silicon substrates through oxygen diffusion. *Materials Sci. Engng. A.* 146 (1991) 51–62.
28. E. P. EerNisse, Viscous flow of thermal SiO_2. *Appl. Phys. Lett.* 30 (1977) 290–293.
29. D. Chin, S.-Y. Oh, S.-M. Hu, R. W. Dutton and J. L. Moll, Two-dimensional oxidation. *IEEE Trans. Electron Dev. ED*-30 (1983) 744–749.

30. L. O. Wilson and R. B. Marcus, Oxidation of curved silicon surfaces. *J. Electrochem. Soc.* 134 (1987) 481–490.
31. E. Bassous, H. N. Yu and V. Maniscalco, Topology of silicon structures with recessed SiO_2. *J. Electrochem. Soc.* 123 (1976) 1729–1737.
32. A. Bohg and A. K. Gaind, Influence of film stress and thermal oxidation on the generation of dislocations in silicon. *Appl. Phys. Lett.* 33 (1978) 895–897.
33. I. Magdo and A. Bohg, Framed recessed oxide scheme for dislocation-free planar Si structures. *J. Electrochem. Soc.* 125 (1978) 932–936.
34. S. Isomae, Y. Tamaki, A. Yajima, M. Nanba and M. Maki, Dislocation generation at Si_3N_4 film edges on silicon substrates and viscoelastic behaviour of SiO_2 films. *J. Electrochem. Soc.* 126 (1979) 1014–1019.
35. K. Shibata and K. Taniguchi, Generation mechanism of dislocations in local oxidation of silicon. *J. Electrochem. Soc.* 127 (1980) 1383–1387.
36. Y. Tamaki, S. Isomae, S. Mizuo and H. Higuchi, Evaluation of dislocation generation at Si_3N_4 film edges on silicon substrates by selective oxidation. *J. Electrochem. Soc.* 128 (1981) 644–648.
37. Y. Tamaki, S. Isomae, S. Mizuo and H. Higuchi, Evaluation of dislocation generation on silicon substrates by selective oxidation. *J. Electrochem. Soc.* 130 (1983) 2266–2270.
38. T. L. Tung and D. A. Antoniadis, A boundary integral equation approach to oxidation modeling. *IEEE Trans. Electron Dev. ED*-32 (1985) 1954–1959.
39. R. Singh, N. E. McGruer, K. Rajkanan and J. H. Weiss, A new growth enhancement in thin SiO_2 formed by rapid isothermal oxidation of silicon. *J. Vac. Sci. Technol. A.* 6 (1988) 1480–1483.
40. Y.-L. Chiou, C. H. Sow K. Ports, Generalized linear-parabolic law: A mathematical model for thermal oxidation of silicon. *IEEE Electron Dev. Lett.* 10 (1989) 1–3.
41. C. K. Huang and R. J. Jaccodine, Impurity dependence of film-edge-induced dislocations in silicon. *J. Appl. Phys.* 66 (1989) 531–535.
42. H. Umimoto and S. Odanaka, Three-Dimensional numerical simulation of local oxidation of silicon. *IEEE Trans. Electron Dev.* 38 (1991) 505–511.
43. P. U. Kenkare, C. Mazuré, J. D. Hayden, J. R. Pfiester, J. Ko, H. C. Kirsch, S. A. Ajuria, P. Crabtree and T. Vuong, Scaling of poly-encapsulated LOCOS for $0.35\mu m$ CMOS technology. *IEEE Trans. Electron Dev.* 41 (1994) 56–62.
44. T. Park, S. J. Ahn and S. T. Ahn, A Novel Local Oxidation of Silicon (LOCOS)-Type Isolation Technology Free of the Field Oxide Thinning Effect. *Jpn. J. Appl. Phys.* 33 (1994) 435–439.
45. E. A. Irene, E. Tierney and J. Angilello, A viscous flow model to explain the appearance of high density thermal SiO_2 at low oxidation temperatures. *J. Electrochem. Soc.* 129 (1982) 2594–2597.
46. E. P. EerNisse, Stress in thermal SiO_2 during growth. *Appl. Phys. Lett.* 35 (1979) 8–10.
47. T. Y. Tan and U. Gösele, Growth kinetics of oxidation-induced stacking faults in silicon: A new concept. *Appl. Phys. Lett.* 39 (1981) 86–88.
48. W. A. Tiller, On the kinetics of the thermal oxidation of silicon. IV. The two-layer film. *J. Electrochem. Soc.* 130 (1983) 501–506.
49. T.-C. Wu, W. T. Stacy and K. N. Ritz, The influence of the LOCOS processing parameters on the shape of the bird's beak structure. *J. Electrochem. Soc.* 130 (1983) 1563–1566.
50. R. B. Marcus and T. T. Sheng, The oxidation of shaped silicon surfaces. *J. Electrochem. Soc.* 129 (1982) 1278–1282.
51. M. Morita and T. Ohmi, Characterization and Control of Native Oxide on Silicon. *Jpn. J. Appl. Phys.* 33 (1994) 370–374.
52. J. Vanhellemont and C. Claeys, A quantitative model for silicon yield stress calculations at thin film edges. *J. Electrochem. Soc.* 135 (1988) 1509–1517.
53. H. Matsumoto and M. Fukuma, Numerical modeling of nonuniform Si thermal oxidation. *IEEE Trans. Electron Dev. ED*-32 (1985) 132–140.
54. S. Isomae, Oxidation-induced stress in a LOCOS structure. *IEEE Electron Dev. Lett. EDL*-7 (1986) 368–370.
55. D.-B. Kao, J. P. McVittie, W. D. Nix and K. C. Saraswat, Two-dimensional thermal oxidation of silicon–II. Experiments. *IEEE Trans. Electron Dev. ED*-35 (1988) 25–37.
56. P. Sutardja and W. G. Oldham, Modeling of stress effects in silicon oxidation. *IEEE Trans. Electron Dev. ED*-36 (1989) 2415–2421.